

# Stabilizer Scars

Jeremy Hartse,<sup>1,\*</sup> Lukasz Fidkowski,<sup>2</sup> and Niklas Mueller<sup>1</sup>

<sup>1</sup>*InQubator for Quantum Simulation (IQuS), Department of Physics, University of Washington, Seattle, WA 98195, USA.*

<sup>2</sup>*Department of Physics, University of Washington, Seattle, WA 98195, USA.*

Quantum many-body scars are eigenstates in non-integrable isolated quantum systems that defy typical thermalization paradigms, violating the eigenstate thermalization hypothesis and quantum ergodicity. We identify exact analytic scar solutions in a 2 + 1 dimensional lattice gauge theory in a quasi-1d limit as zero-magic stabilizer states. We propose a protocol for their experimental preparation, presenting an opportunity to demonstrate a quantum over classical advantage via simulating the non-equilibrium dynamics of a strongly coupled system. Our results also highlight the importance of magic for gauge theory thermalization, revealing a connection between computational complexity and quantum ergodicity.

*Introduction.*— Unprecedented advances in controlling isolated quantum systems [1–3] have enabled the study of non-equilibrium phenomena in complex many-body systems, including thermalization, a pivotal subject in many fields [4–7]. According to the eigenstate thermalization hypothesis (ETH) [8, 9], non-integrable isolated systems thermalize, with quantum ergodicity ensuring that states explore a vast Hilbert space regardless of the initial state.

However, recent experiments have identified so-called *quantum many-body scars* (QMBS), where quantum ergodicity and the ETH are violated despite the system being strongly coupled and non-integrable [10–13]. This has sparked significant theoretical and experimental interest [14–39], but many questions are still open: For instance, the analytic mechanisms behind QMBS, their stability in the thermodynamic limit and their fate as generic phenomena, beyond finely-engineered synthetic quantum systems, or use in quantum information and computing, are presently unclear.

Seeking insight into the mechanisms behind QMBS, in this Letter we investigate a quasi-1d limit of a strongly coupled and non-integrable 2+1d model of a lattice gauge theory (LGT). LGTs are an important target for quantum simulators and computers because of their relevance in high-energy and nuclear physics [40–44], where thermalization is a central objective [45–48], for topological phases [49, 50], or quantum error correction [51–53].

Our study, based on an Ising-LGT duality and fermionization, uncovers exact analytic scar solutions for arbitrary couplings and in the thermodynamic limit. Importantly, the scar subspace of the model is spanned by certain *stabilizer states* [54, 55] with zero magic [56, 57], revealing a connection between complexity and quantum ergodicity. A key result is an experimental proposal that offers an opportunity to verify a quantum over classical advantage via simulating the non-equilibrium dynamics of a large, strongly coupled system—contrasting scar states, whose dynamics is classically simulable, with non-scar initial states, which are not.

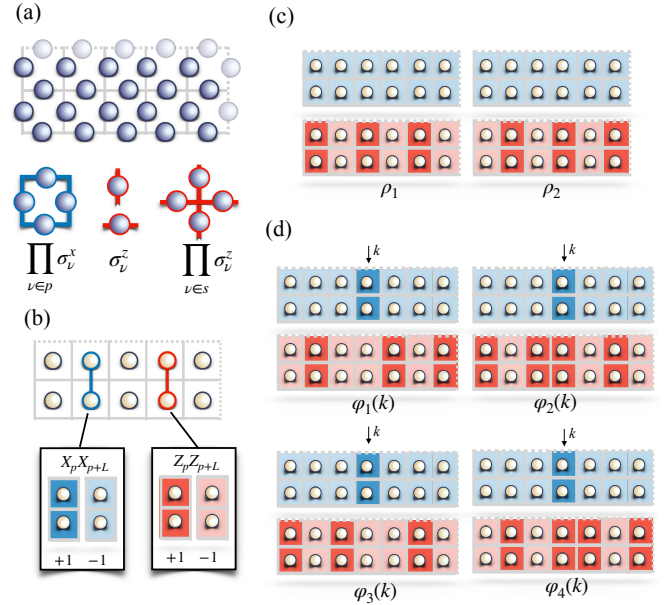


FIG. 1. *Quantum Many-Body Scars in  $\mathbb{Z}_2$  LGT.* (a) Degrees of freedom of  $\mathbb{Z}_2$  LGT on the edges of a (periodic) two-dimensional square lattice; plaquette, electric field and Gauss law operators are shown. (b) Illustration of Dual Ising model with stabilizers  $X_p X_{p+L}$  (eigenvalues in light and dark blue) and  $Z_p Z_{p+L}$  (eigenvalues in light and dark red). (c) QMBS scar solutions of a  $L \times 2$  lattice where  $L$  is even, shown in terms of  $X_p X_{p+L}$  and  $Z_p Z_{p+L}$  eigenvalues. (d) The scar subspace for odd  $L$  is spanned by the states shown.

*Model.*— We consider  $\mathbb{Z}_2$  LGT with Hamiltonian,

$$H = - \sum_p \prod_{\nu \in p} \sigma_\nu^x - g \sum_\nu \sigma_\nu^z \quad (1)$$

where  $\nu$  are the links of a square lattice in 2 + 1 dimensions with periodic boundary conditions, and  $p$  are plaquettes. We consider the combined +1 eigenspace of Gauss' laws,  $G_s \equiv \prod_{\nu \in s} \sigma_\nu^z$ , where  $\nu \in s$  denotes the links  $\nu$  originating from a lattice site  $s$ ; two ribbon operators  $V_{x,y} \equiv \prod_{\nu \in \mathcal{L}_{x/y}} \sigma_\nu^z$ ,  $\mathcal{L}_{x/y}$  wind periodically around  $x/y$  and specify additional symmetries. We consider a

\* jhartse@uw.edu

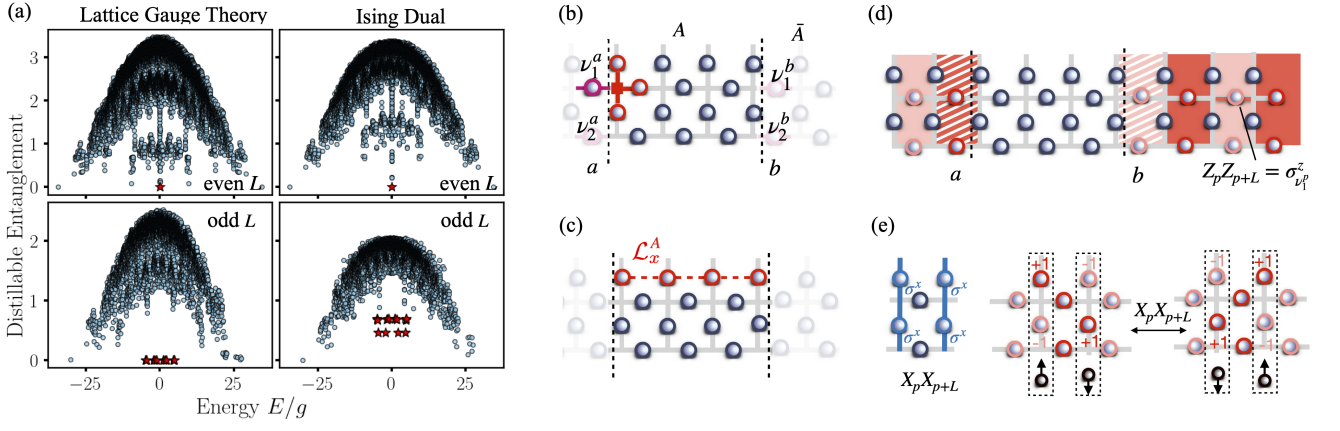


FIG. 2. *Quantum Many-Body Scars: Lattice Gauge Theory vs. Ising Dual.* (a) Top row: Distillable entanglement of all eigenstates for even  $L$ , for  $L = 8$  and  $g = 0.9$ . The scar states, given by Eq. (3) and shown as red stars, appear in both the LGT (left panel) and the dual Ising model (right panel) and are characterized by exactly zero distillable entanglement. Bottom row: For odd  $L$  ( $L = 7$  and  $g = 0.9$ ), the scar eigenstates form linear superpositions of the stabilizer states, Eq. (4). The scars exhibit zero distillable entanglement in the LGT, but not in the dual Ising model. (b) Superselection sectors,  $\sigma_\nu^z = \pm 1$  on each boundary link  $\nu \in \{\nu_1^a, \nu_2^a, \nu_1^b, \nu_2^b\}$ , are associated with Gauss laws. (c) An additional superselection sector,  $\prod_{\nu \sim \mathcal{L}_x^A} \sigma_\nu^z \sim X_a Z_b$ , where  $\mathcal{L}_x^A = \mathcal{L}_x \cap A$ , arises from restricting  $\prod_{\nu \sim \mathcal{L}_x} \sigma_\nu^z = V_x$  to  $A$  (similar for  $\bar{A}$ ). (d) The  $Z_p Z_{p+L}$  eigenvalue configuration, for  $p \leq a$  and  $p \geq b$ , is shown for the state  $|\psi_{+1,-1}\rangle$  from Eq. (11), with a defect trapped inside  $A$ . Along with the  $X_p X_{p+L}$  and Gauss law constraints, the reduced density matrix of  $|\psi_{+1,-1}\rangle$  on  $\bar{A}$  (and  $A$ ) has at most rank 2. The light red and dark red colors indicate the  $Z_p Z_{p+L}$  eigenvalue as in fig 1. (e) While  $Z_p Z_{p+L}$  constrains horizontal links in the LGT, Gauss law eigenstates require vertically separated vertical links to be in either a  $+1, -1$  or  $-1, +1$  configuration, providing an effective spin-1/2 degree of freedom. Imposing the  $X_p X_{p+L}$  constraint leads to two states—one even, one odd under  $\prod_{\nu \sim \mathcal{L}_x^A} \sigma_\nu^z$ —resembling the degenerate ground state of a 1D Ising model without a transverse field.

lattice of  $L \times 2$  plaquette and, w.l.o.g., set  $V_x = V_y = 1$ .

The model described by Eq. (1) is dual to a 2 + 1d transverse-field Ising model with periodic boundary conditions when restricted to the parity-even subspace,  $\prod_p X_p = 1$ , via the map  $X_p \equiv \prod_{\nu \in p} \sigma_\nu^x$  and  $Z_p Z_{p+\hat{a}} = \sigma_\nu^z$ , where  $p$  and  $p + \hat{a}$  are adjacent to  $\nu$ ,

$$H^{\text{dual}} = - \sum_{p=1}^L [X_p + X_{p+L}] - \tilde{g} \sum_{p=1}^L Z_p Z_{p+L} - \sum_{p=1}^L g_p [Z_p Z_{p+1} + Z_{p+L} Z_{p+L+1}], \quad (2)$$

where  $\tilde{g} \equiv g(1 + V_y)$ , and  $g_p \equiv g$  for  $p < L$  and  $g_p = V_x g$  for  $p = L$ . Our notation is such that plaquettes are numbered 1 to  $L$  from left to right in the top row and from  $L + 1$  to  $2L$  from left to right in the bottom row.

*Quantum Many-Body Scars.*— For an arbitrary value of the coupling  $g$ , and  $L \times 2$  geometry, the model's eigenspace possesses a subspace of exact QMBS. For even  $L$ , this subspace is two-dimensional and spanned by the states,

$$\rho_{1/2} \equiv \prod_{p=1}^L \left[ \frac{1 \pm (-1)^p Z_p Z_{p+L}}{2} \right] \left[ \frac{1 - X_p X_{p+L}}{2} \right] \quad (3)$$

where  $\rho_{1/2} \equiv |\Psi_{1/2}\rangle \langle \Psi_{1/2}|$  are (eigen-)states with exactly zero energy,  $H|\Psi_{1/2}\rangle = 0$ . In Supplemental Material [58], we derive Eq. (3).

Importantly, Eq. (3) are *stabilizer states*, specified by the eigenvalues of  $X_p X_{p+L}$  and  $Z_p Z_{p+L}$ . The corresponding scar states in LGT formulation are obtained upon replacing  $X_p X_{p+L} = \prod_{\nu \in p} \sigma_\nu^x \sigma_{\nu+L}^x$  and  $Z_p Z_{p+L} = \sigma_\nu^z$ ; additionally, on this side of the duality, Gauss's laws (and  $V_x, V_y$ ) are stabilizers, i.e.,

$$\rho_{1/2} \rightarrow \rho_{1/2} \prod_s \left[ \frac{1 + G_s}{2} \right] \frac{1 + V_x}{2} \frac{1 + V_y}{2}, \quad (4)$$

where the l.h.s. is the Ising and the r.h.s. the LGT expression. For brevity, we also use  $X_p X_{p+L}$  and  $Z_p Z_{p+L}$  when discussing the LGT, referring to  $\prod_{\nu \in p} \sigma_\nu^x \sigma_{\nu+L}^x$  and  $\sigma_\nu^z$ , respectively.

For odd  $L$ , the scar subspace is spanned by  $4L$  stabilizer states,  $\varphi_\alpha \equiv |\varphi_\alpha\rangle \langle \varphi_\alpha|$ ,

$$\varphi_\alpha(k) \equiv \prod_{q < k} \left[ \frac{1 + s_\alpha (-1)^{k-q} Z_q Z_{q+L}}{2} \right] \frac{1 + t_\alpha Z_k Z_{k+L}}{2} \times \prod_{q > k} \left[ \frac{1 - s_\alpha (-1)^{k-q} Z_q Z_{q+L}}{2} \right] \Phi(k). \quad (5)$$

Here,  $\alpha = 1, 2, 3, 4$  and  $k = 1, \dots, L$ ; furthermore we abbreviate  $s_1 = s_4 \equiv 1$ ,  $s_2 = s_3 \equiv -1$ , as well as  $t_2 \equiv t_4 \equiv 1$  and  $t_1 = t_3 \equiv -1$ . Additionally,

$$\Phi(k) \equiv \prod_{q \neq k} \left[ \frac{1 - X_q X_{q+L}}{2} \right] \frac{1 + X_k X_{k+L}}{2}. \quad (6)$$

Unlike for even  $L$ , Eq. (5) are not eigenstates, but rather they define a conserved subspace in which the action of  $H$  maps scar states onto other scar states exactly while having zero overlap with non-scar states; we demonstrate this property in Supplemental Material [58]. The states in the LGT formulation are defined analogously to Eq. (4), with Gauss laws and  $V_x, V_y$  additional stabilizers.

*Entanglement and Magic.*— The scar basis states, Eq. (3) and Eq. (5), have zero magic because they are stabilizer states. We investigate their entanglement, focusing on the von Neumann entanglement entropy of a bipartition along the long ( $L$ ) lattice direction,  $\rho_A = \text{Tr}_{\bar{A}}(\rho)$ , where  $A$  is the subsystem and  $\bar{A}$  its complement. The reduced density matrix  $\rho_A \equiv \bigoplus_s \rho_A^{(s)}$  exhibits a block-diagonal structure, whose origin we explain below. As a result, the von Neumann entanglement entropy can be decomposed into distillable and symmetry contributions,

$$S_{\text{vN}} = S_{\text{vN}}^{\text{dist}} - \sum_s p_s \log(p_s), \quad (7)$$

where the distillable von Neumann entropy is

$$S_{\text{vN}}^{\text{dist}} = \sum_s p_s S_{\text{vN}}^{(s)}, \quad S_{\text{vN}}^{(s)} = -\text{Tr}(\tilde{\rho}_A^{(s)} \log(\tilde{\rho}_A^{(s)})), \quad (8)$$

with  $\tilde{\rho}_A^{(s)} \equiv \rho_A^{(s)}/p_s$  and  $p_s = \text{Tr}(\rho_A^{(s)})$ . Although the LGT and Ising models are dual to each other, the symmetries of  $\rho_A$  and its entanglement structure generally differ between the two formulations.

In the top row of Fig. 2(a) we show the distillable entanglement for even  $L = 8$  and  $g = 0.9$  in both the LGT (left panel) and the Ising model (right panel). For both zero-energy scar eigenstates, the distillable entanglement vanishes. In contrast, the bottom row illustrates the same quantity for *odd*  $L = 7$ . Here, the eigenstates are linear superpositions of the stabilizer scar solutions, Eq. (5). In the LGT, the distillable entanglement remains zero for any coupling, whereas it is non-zero in the Ising dual.

*Zero distillable entanglement in lattice gauge theory scar states.*— The conserved scar subspace exists in both the Ising model and the LGT, but the scars' distillable entanglement is *exactly zero for any value of coupling* only in the LGT owing to the special superselection sector structure in the latter. To explain this structure, we consider the entanglement cut shown in Fig. 2(b). Gauss' law implies that  $\sigma_\nu^z = \pm 1$  on each boundary link  $\nu \in \{\nu_1^a, \nu_2^a, \nu_1^b, \nu_2^b\}$  is a distinct superselection operator. However, the constraint  $\prod_{\nu \sim \mathcal{L}_y} \sigma_\nu^z = V_y = 1$ , where  $\mathcal{L}_y$  is any non-trivial loop in the  $y$  direction and  $\nu \sim \mathcal{L}_y$  are the links cut by  $\mathcal{L}_y$ , gives  $\sigma_{\nu_1^{a/b}}^z \sigma_{\nu_2^{a/b}}^z = 1$ . Consequently, there is only one superselection operator  $\sigma_{\nu_1^{a/b}}^z$  associated with each boundary, which in the Ising dual equal  $Z_a Z_{a+L}$  and  $Z_b Z_{b+L}$ . A third superselection operator arises from the constraint  $\prod_{\nu \sim \mathcal{L}_x} \sigma_\nu^z = V_x = 1$ . Its restriction to  $A$ , shown in Fig. 2(c),  $\prod_{\nu \sim \mathcal{L}_x^A} \sigma_\nu^z \sim Z_a Z_b$ ,

where  $\mathcal{L}_x^A = \mathcal{L}_x \cap A$ , gives the third superselection operator. We refer to Supplemental Material [58] for more details.

Let us now explain why these three superselection operators result in zero distillable entanglement for the scar energy eigenstates in the LGT (but not for the Ising dual). The argument presented is for the case of odd  $L$  (even  $L$  is easier). Using the notation of Fig. 1(d), a scar energy eigenstate is a superposition

$$|\psi\rangle = \sum_{1 \leq k \leq L, 1 \leq i \leq 4} c_{k,i} |\phi_i(k)\rangle \quad (9)$$

where  $\sum_{k,i} |c_{k,i}|^2 = 1$  and  $|\phi_i(k)\rangle$  is a LGT scar basis state via our dictionary. We now group the terms in this superposition according to their boundary superselection sectors

$$|\psi\rangle = \sum_{\alpha, \beta = \pm 1} |\psi_{\alpha, \beta}\rangle, \quad (10)$$

i.e.,  $Z_a Z_{a+L} |\psi_{\alpha, \beta}\rangle = \alpha |\psi_{\alpha, \beta}\rangle$  and  $Z_b Z_{b+L} |\psi_{\alpha, \beta}\rangle = \beta |\psi_{\alpha, \beta}\rangle$ . The key observation is that, when considering a reduced density matrix on  $A$ , the four terms fall into separate superselection sectors.

Since the argument is nearly identical for all four states  $|\psi_{\alpha, \beta}\rangle$ , we will demonstrate it for  $\alpha = 1$  and  $\beta = -1$  and  $a$  and  $b$  are even. We consider

$$\begin{aligned} |\psi_{+1, -1}\rangle &= \sum_{(a < k < b) \text{ and } (k \text{ even}), i=1,4} c_{k,i} |\phi_i(k)\rangle \\ &+ \sum_{(a < k < b) \text{ and } (k \text{ odd}), i=2,3} c_{k,i} |\phi_i(k)\rangle \\ &+ c_{a,4} |\phi_4(a)\rangle + c_{b,1} |\phi_1(b)\rangle \end{aligned} \quad (11)$$

which represents a state where the  $Z_k Z_{k+L}$  defect, as illustrated in Fig. 1(d), is trapped within region  $A$  — the set-up is shown in Fig. 2(d). Any state described by Eq. (11) shares the same stabilizer values for  $X_p X_{p+L}$  and  $Z_p Z_{p+L}$  for all  $p \leq a$  and  $p \geq b$  [59]. Fixing the stabilizer values  $X_p X_{p+L}$  and  $Z_p Z_{p+L}$  for all  $p \leq a$  and  $p \geq b$  imposes  $2(L - b + a - 1)$  constraints. Additionally, enforcing Gauss's law in the complement region introduces  $2(L - b + 1) - 1$  further constraints. For given  $\alpha$  and  $\beta$ , there are  $4(L + a - b) - 2$  qubits in the complement, leaving exactly one remaining spin degree of freedom. Consequently, the reduced density matrix of the state  $|\psi_{+1, -1}\rangle$  of both the complement and  $A$  has at most rank 2. Furthermore, as explained in Fig. 2(e), these two states differ in their eigenvalues of  $\prod_{\nu \sim \mathcal{L}_x, \nu \in \bar{A}} \sigma_\nu^z$ . As a result, the distillable entanglement of an arbitrary superposition is zero.

In contrast, the only symmetry present in the transverse Ising model is the global spin-flip symmetry, which gives rise to *two* superselection sectors. Within each sector, it is possible to construct entangled superpositions of the scar states. This aligns with numerical results in Fig. 2(a) for odd  $L$ , which show that the scar eigenstates

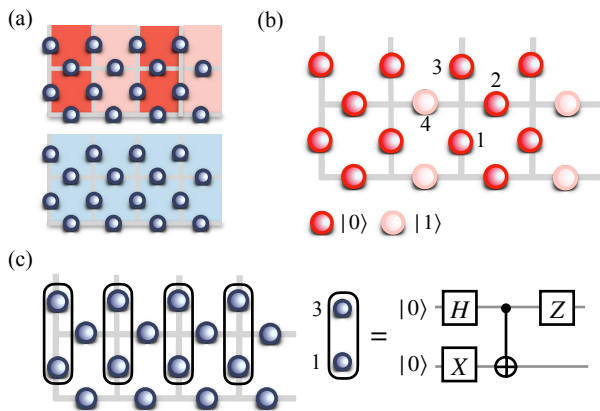


FIG. 3. *QMBS Preparation.* (a) Example of a scar basis state specified by the eigenvalues of  $X_p X_{p+L}$  and  $Z_p Z_{p+L}$ . (b) Initial state for the preparation algorithm in the LGT formulation ( $V_y = 1$ ). Horizontal links are initialized in  $\sigma^z$  (electric) eigenstates, while vertical links are initially set to  $|0\rangle$ . (c) The state preparation circuit operates on pairs of vertically separated qubits located at  $\nu$  and  $\nu + \hat{y}$ . An example is shown where the circuit prepares a state with  $\sigma_\nu^x \sigma_{\nu+\hat{y}}^x = -1$  and  $\sigma_\nu^z \sigma_{\nu+\hat{y}}^z = -1$ ; combined with the horizontal links, this yields a Gauss law  $+1$  eigenstate. Minor circuit adjustments enable preparation of any combination of  $\sigma_\nu^x \sigma_{\nu+\hat{y}}^x = \pm 1$  and  $\sigma_\nu^z \sigma_{\nu+\hat{y}}^z = \pm 1$  states, allowing access to any scar subspace basis state. The circuit maintains product-state structure along  $L$ ; each state remains a 2-qubit product state.

in the Ising model exhibit non-zero—and not insignificantly small—distillable entanglement.

*Generating Algebra.*— As is shown in Supplemental Material [58], the scar subspace is preserved not just by  $H$ , but also by the individual terms  $X_p + X_{p+L}$ ,  $Z_p Z_{p+1} + Z_{p+L} Z_{p+L+1}$ , and  $Z_p Z_{p+L}$  appearing in  $H$ . Following [60, 61] we denote the algebra generated by these terms as  $\mathcal{A}$ , and its commutant - that is, the algebra of all operators that commute with all operators in  $\mathcal{A}$  in the endomorphism algebra of the full Hilbert space - as  $\mathcal{C}$ . As demonstrated in [61], the existence of QMBS is reflected in a non-trivial commutant  $\mathcal{C}$ . Indeed, one can find a basis in which all elements of  $\mathcal{C}$  share the same block diagonal form, and the scar subspace corresponds to a particular block.

We compute the commutant  $\mathcal{C}$  in the two leg transverse field Ising ladder by using a fermionic representation of the operator algebra introduced in the Supplemental Material [58]. Here, we give a brief overview of the argumentation: this representation comes about from applying the ordinary Jordan-Wigner (JW) transformation from left to right along the first row (sites  $1, \dots, L$ ), and then along the second row (sites  $L+1, \dots, 2L$ ). The two-level fermionic system at each site  $p = 1, \dots, 2L$  can be described using two Majorana operators  $\gamma_p, \tilde{\gamma}_p$ , which can then be recombined into complex fermions  $c_p, c_p^\dagger$  and  $\tilde{c}_p, \tilde{c}_p^\dagger$ ,  $p = 1, \dots, L$  by  $c_p = \frac{1}{2}(\gamma_p - i\tilde{\gamma}_{p+L})$ ,  $\tilde{c}_p = \frac{1}{2}(\tilde{\gamma}_p - i\gamma_{p+L})$ . The virtue of this representation is that two of the three types of terms generat-

ing  $\mathcal{A}$  fermionize into manifestly particle number,  $\hat{N} = \sum_{p=1}^L (c_p^\dagger c_p + \tilde{c}_p^\dagger \tilde{c}_p)$ , conserving operators quadratic in the fermions:  $X_p + X_{p+L} \rightarrow 2i(c_p \tilde{c}_p^\dagger + c_p^\dagger \tilde{c}_p)$  and  $Z_p Z_{p+1} + Z_{p+L} Z_{p+L+1} \rightarrow 2i(\tilde{c}_p c_{p+1}^\dagger + \tilde{c}_p^\dagger c_{p+1})$  (for  $p < L$ ). As shown in the Supplemental Material [58], the remaining terms,  $Z_p Z_{p+L}$  and  $Z_1 Z_L + Z_{L+1} Z_{2L}$ , fermionize to operators that include a residual JW string, exhibiting a particle-hole symmetry that conjugates  $\hat{N}$  to  $2L - \hat{N}$ . This implies that  $(\hat{N} - L)^2$  commutes with these terms and, therefore, with all of  $\mathcal{A}$ , making it an element of  $\mathcal{C}$ . In fact,  $(\hat{N} - L)^2$  generates the entirety of  $\mathcal{C}$ , as follows from Table II of [62]. In terms of the commutant  $\mathcal{C}$ , for the even  $L$  scar subspace the fermionic dual has overall even fermion parity, and the two scar states correspond to  $(\hat{N} - L)^2 = L^2$ , i.e. the all empty  $\hat{N} = 0$  and the completely filled  $\hat{N} = 2L$  states. For odd  $L$  the fermionic dual has odd fermion parity, and hence the least degenerate eigenspace of  $(\hat{N} - L)^2$  corresponds to the eigenvalue  $(L - 1)^2$ , has dimension  $4L$ , and is spanned by the one-particle and one-hole states.

We note that the scars identified here differ from those in Ref. [63], where an exact low-entanglement scar state,  $|\psi'_{E=0}\rangle$ , was constructed as a tensor product over ‘diagonal’ singlets (Eq. 8 in Ref. [63]). This state, while an eigenstate of the two-leg transverse field Ising model, lies outside the scar subspaces computed in this work. In particular, the state  $|\psi'_{E=0}\rangle$  is not robust against translation symmetry breaking in the  $x$ -direction, as opposed to the scar subspaces found in this work.

*Experimental Realization.*— Finally, we propose an experimental implementation by time-evolving a scar stabilizer basis state in the LGT, versus preparing a non-scar state. Importantly, since the scar subspace is exactly decoupled from the rest of the Hilbert space, an initial scar state is constrained to explore only a polynomially small subspace of  $4L$  states, as opposed to a non-scar state, which may probe the exponentially large  $2^{2L-1}$  dimensional Hilbert space. Focusing on odd  $L$ , our goal is to prepare one of the basis states illustrated in Fig. 1(d), which is a simultaneous eigenstate of  $Z_p Z_{p+L}$ ,  $X_p X_{p+L}$ , and the Gauss law operators. The state preparation protocol is outlined in Fig. 3, with Fig. 3(a) showing a sample target state with well-defined  $Z_p Z_{p+L}$  and  $X_p X_{p+L}$  eigenvalues. This is achieved by configuring the horizontal and vertical links as depicted in Fig. 3(b), followed by the algorithm shown in Fig. 3(c) which shows that the scar basis states are 2-qubit product states. Non-scar initial states are randomly drawn ( $z$ -basis) product states that are consistent with Gauss law. By monitoring the  $Z_p Z_{p+L}$  eigenvalues of these states we ensure there is zero overlap with the scar subspace.

We focus on two observables that distinctly differentiate scar dynamics from non-scar dynamics: the overlap between the initial and time-evolved state, known as the Loschmidt echo

$$L(t; |\psi_0\rangle) \equiv \langle \psi_0 | \exp\{-iHt\} | \psi_0 \rangle, \quad (12)$$



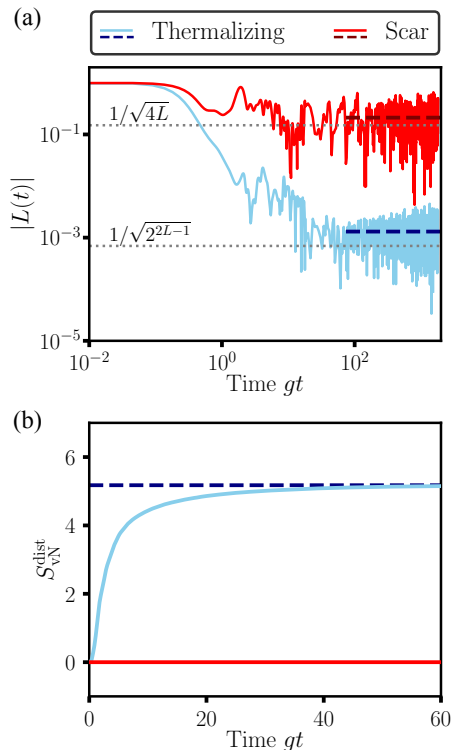


FIG. 4. *Experimental Realization.* (a) The absolute value of the Loschmidt echo,  $|L(t)|$ , is shown as a function of time, comparing an initial state within the scar subspace (red lines) to a thermalizing state (blue lines) for system size  $L = 11$ . The time-averaged value at late times is indicated by the dark red dashed line for the scar state. The scar echo decays as  $|L(t)| \sim 1/\sqrt{4L}$  (gray dotted line), where  $4L$  is the size of the scar subspace. In contrast, the thermalizing state (blue lines) explores a much larger Hilbert space. For a random circuit that fully explores this space,  $|L(t)|$  would decay to  $|L(t)| \sim 1/\sqrt{2^{2L-1}}$  (gray dotted lines), however, due to energy conservation, the thermalizing state's late-time average (dark blue dashed line) remains slightly above this value. (b) The distillable entanglement  $S_{vN}^{\text{dist}}$  of a time-evolved scar state (red) remains zero throughout. By contrast, for a thermalizing state (light blue),  $S_{vN}^{\text{dist}}$  increases over time until reaching a constant, non-zero saturation value (blue dashed line).

and the distillable von Neumann entropy defined in Eq. (8). While exact time evolution is performed here, in an experimental setting one would typically employ Trotterized time evolution—for an alternative scheme that avoids it see [58].

In Fig. 4(a), we plot the absolute value  $|L(t)|$  as a function of time for one of the  $4L$  scar basis states (solid red lines) for  $L = 11$ . For comparison, we also show the dynamics of a non-scar initial state (solid blue lines). The evolution of scar versus non-scar states differ dramatically. In the polynomially small scar subspace the Loschmidt echo decays to  $|L(t)| \sim 1/\sqrt{4L}$ . However, no full revivals are observed, as the energies of eigenstates in the scar subspace are not equidistant. In contrast,

non-scar initial states exhibit quantum ergodic behavior, where the initial state explores the (exponentially large) full Hilbert space that is available to it based on energy conservation [64]. Eventually, this state thermalizes, with the Loschmidt echo decaying to a much lower value. For comparison, we show  $|L(t)| \sim 1/\sqrt{2^{2L-1}}$ , the saturation value in the absence of energy conservation. Loschmidt echos can be measured in experiment using ancilla-based interferometry [65–67].

Fig. 4(b) shows the distillable entanglement, revealing an even more striking difference between scar and non-scar sectors. In the scar sector, the distillable entanglement remains exactly zero at all times, consistent with the argument presented earlier. In contrast, for states outside the scar subspace, the distillable entanglement increases over time, indicating that the system is thermalizing. Using random-measurement tools [68], for the model at hand, (distillable) entanglement can be measured directly [69], or see [48] for an experimental demonstration via entanglement Hamiltonian tomography [70, 71].

*Conclusions.*— In this Letter, we identified exact quantum many-body scars in a quasi-1d limit of a 2+1 dimensional  $\mathbb{Z}_2$  LGT, for arbitrary coupling, that are based on zero-magic stabilizer states. An Ising-LGT duality and mapping onto a fermionic representation allowed us to analytically show their existence via a non-trivial commutant of the algebra generated by the Hamiltonian terms which we explicitly compute. Notably, in the gauge theory formulation, scar states—and arbitrary superpositions—always have *zero distillable entanglement*.

Complexity is a useful measure in various physical systems [72–78]: Our finding reveals a connection between computational complexity and quantum ergodicity. Additionally, it indicates that identifying QMBS through entanglement may be unreliable: If we had computed only the (total) von Neumann entropy, instead of the *distillable* entanglement, we likely would not have initially detected these states. Furthermore, even the *distillable entanglement* is basis-dependent, differing between the LGT and the Ising dual. In contrast, while not explicitly computed, the QMBS subspace can be distinguished from generic states, i.e., those that obey the ETH and exhibit quantum ergodicity, through measures of magic such as stabilizer Rényi entropies (SRE) [79]. In particular, we highlight [80], which investigates SREs of scarred states in the PXP model. Specifically, typical states have magic that scales *linearly* with  $L$  [79, 81], whereas the magic of states in the scar subspace is constrained by the superpositions that can be formed among the  $4L$  zero-magic states. Based on arguments presented in [79], we conjecture that the magic of states within the scar subspace is at most *logarithmic in  $L$*  [82].

The experimental realization we propose may serve as a blueprint for demonstrating a quantum advantage over classical computation: Whether a system is classically simulable or intractable depends solely on the initial state but not on the quantum circuit for time evolution, which

is the same in each case. If the initial state originates from the scar subspace, the time evolution is classically computable, even for extremely large  $L$ . This enables the demonstration of a quantum computation at scale being reliable, i.e., having sufficiently low decoherence and error rates for it to be impossible to be classically emulatable. Establishing a quantum advantage would then consist of repeating the same computation but with a generic thermalizing non-scar initial state, which *cannot*

*be classically computed* except for very small  $L$ .

*Acknowledgements.*— We thank Marc Illa, Martin Savage, and Nikita Zemlevskiy for discussions. J.H. and N.M. acknowledge funding by the DOE, Office of Science, Office of Nuclear Physics, IQUS (<https://iqus.uw.edu>), via the program on Quantum Horizons: QIS Research and Innovation for Nuclear Science under Award DE-SC0020970. L.F. is supported by NSF DMR-2300172.

- 
- [1] C. Gross and I. Bloch, Quantum simulations with ultracold atoms in optical lattices, *Science* **357**, 995 (2017).
- [2] A. Browaeys and T. Lahaye, Many-body physics with individually controlled rydberg atoms, *Nature Physics* **16**, 132 (2020).
- [3] E. Altman, K. R. Brown, G. Carleo, L. D. Carr, E. Demler, C. Chin, B. DeMarco, S. E. Economou, M. A. Eriksson, K.-M. C. Fu, *et al.*, Quantum simulators: Architectures and opportunities, *PRX quantum* **2**, 017003 (2021).
- [4] J. Eisert, M. Friesdorf, and C. Gogolin, Quantum many-body systems out of equilibrium, *Nature Physics* **11**, 124 (2015).
- [5] L. D’Alessio, Y. Kafri, A. Polkovnikov, and M. Rigol, From quantum chaos and eigenstate thermalization to statistical mechanics and thermodynamics, *Advances in Physics* **65**, 239 (2016).
- [6] M. Ueda, Quantum equilibration, thermalization and prethermalization in ultracold atoms, *Nature Reviews Physics* **2**, 669 (2020).
- [7] J. Berges, M. P. Heller, A. Mazeliauskas, and R. Venugopalan, Qcd thermalization: Ab initio approaches and interdisciplinary connections, *Reviews of Modern Physics* **93**, 035003 (2021).
- [8] J. M. Deutsch, Quantum statistical mechanics in a closed system, *Physical review a* **43**, 2046 (1991).
- [9] M. Srednicki, Chaos and quantum thermalization, *Physical review e* **50**, 888 (1994).
- [10] C. J. Turner, A. A. Michailidis, D. A. Abanin, M. Serbyn, and Z. Papić, Weak ergodicity breaking from quantum many-body scars, *Nature Physics* **14**, 745 (2018).
- [11] M. Serbyn, D. A. Abanin, and Z. Papić, Quantum many-body scars and weak breaking of ergodicity, *Nature Physics* **17**, 675 (2021).
- [12] S. Moudgalya, B. A. Bernevig, and N. Regnault, Quantum many-body scars and hilbert space fragmentation: a review of exact results, *Reports on Progress in Physics* **85**, 086501 (2022).
- [13] A. Chandran, T. Iadecola, V. Khemani, and R. Moessner, Quantum many-body scars: A quasiparticle perspective, *Annual Review of Condensed Matter Physics* **14**, 443 (2023).
- [14] N. Srivatsa, J. Wildeboer, A. Seidel, and A. E. Nielsen, Quantum many-body scars with chiral topological order in 2d and critical properties in 1d, arXiv preprint arXiv:2009.03923.
- [15] C. Turner, A. Michailidis, D. Abanin, M. Serbyn, and Z. Papić, Quantum scarred eigenstates in a rydberg atom chain: Entanglement, breakdown of thermalization, and stability to perturbations, *Physical Review B* **98**, 155134 (2018).
- [16] S. Moudgalya, S. Rachel, B. A. Bernevig, and N. Regnault, Exact excited states of nonintegrable models, *Physical Review B* **98**, 235155 (2018).
- [17] S. Moudgalya, N. Regnault, and B. A. Bernevig, Entanglement of exact excited states of affleck-kennedy-lieb-tasaki models: Exact results, many-body scars, and violation of the strong eigenstate thermalization hypothesis, *Physical Review B* **98**, 235156 (2018).
- [18] S. Choi, C. J. Turner, H. Pichler, W. W. Ho, A. A. Michailidis, Z. Papić, M. Serbyn, M. D. Lukin, and D. A. Abanin, Emergent su(2) dynamics and perfect quantum many-body scars, *Physical review letters* **122**, 220603 (2019).
- [19] N. Shiraiishi, Connection between quantum-many-body scars and the affleck–kennedy–lieb–tasaki model from the viewpoint of embedded hamiltonians, *Journal of Statistical Mechanics: Theory and Experiment* **2019**, 083103 (2019).
- [20] M. Schecter and T. Iadecola, Weak ergodicity breaking and quantum many-body scars in spin-1 x y magnets, *Physical review letters* **123**, 147201 (2019).
- [21] T. Iadecola and M. Žnidarič, Exact localized and ballistic eigenstates in disordered chaotic spin ladders and the fermi-hubbard model, *Physical Review Letters* **123**, 036403 (2019).
- [22] S. Ok, K. Choo, C. Mudry, C. Castelnovo, C. Chamon, and T. Neupert, Topological many-body scar states in dimensions one, two, and three, *Physical Review Research* **1**, 033144 (2019).
- [23] S. Chattopadhyay, H. Pichler, M. D. Lukin, and W. W. Ho, Quantum many-body scars from virtual entangled pairs, *Physical Review B* **101**, 174308 (2020).
- [24] N. Shibata, N. Yoshioka, and H. Katsura, Onsager’s scars in disordered spin chains, *Physical Review Letters* **124**, 180604 (2020).
- [25] K. Lee, R. Melendrez, A. Pal, and H. J. Changlani, Exact three-colored quantum scars from geometric frustration, *Physical Review B* **101**, 241111 (2020).
- [26] T. Iadecola and M. Schecter, Quantum many-body scar states with emergent kinetic constraints and finite-entanglement revivals, *Physical Review B* **101**, 024306 (2020).
- [27] B. van Voorden, J. Minář, and K. Schoutens, Quantum many-body scars in transverse field ising ladders and beyond, *Physical Review B* **101**, 220305 (2020).
- [28] K. Pakrouski, P. N. Pallegar, F. K. Popov, and I. R. Klebanov, Many-body scars as a group invariant sector of hilbert space, *Physical review letters* **125**, 230602 (2020).

- [29] C.-J. Lin, V. Calvera, and T. H. Hsieh, Quantum many-body scar states in two-dimensional rydberg atom arrays, *Physical Review B* **101**, 220304 (2020).
- [30] D. K. Mark, C.-J. Lin, and O. I. Motrunich, Unified structure for exact towers of scar states in the affleck-kennedy-lieb-tasaki and other models, *Physical Review B* **101**, 195131 (2020).
- [31] S. Moudgalya, E. O'Brien, B. A. Bernevig, P. Fendley, and N. Regnault, Large classes of quantum scarred hamiltonians from matrix product states, *Physical Review B* **102**, 085120 (2020).
- [32] I. Mondragon-Shem, M. G. Vavilov, and I. Martin, Fate of quantum many-body scars in the presence of disorder, *PRX Quantum* **2**, 030349 (2021).
- [33] J. Wildeboer, A. Seidel, N. Srivatsa, A. E. Nielsen, and O. Erten, Topological quantum many-body scars in quantum dimer models on the kagome lattice, *Physical Review B* **104**, L121103 (2021).
- [34] B. Windt and H. Pichler, Squeezing quantum many-body scars, *Physical Review Letters* **128**, 090606 (2022).
- [35] Z. Yao, L. Pan, S. Liu, and H. Zhai, Quantum many-body scars and quantum criticality, *Physical Review B* **105**, 125123 (2022).
- [36] I.-C. Chen, B. Burdick, Y. Yao, P. P. Orth, and T. Iadecola, Error-mitigated simulation of quantum many-body scars on quantum computers with pulse-level control, *Physical Review Research* **4**, 043027 (2022).
- [37] Z. Sun, F. K. Popov, I. R. Klebanov, and K. Pakrouski, Majorana scars as group singlets, *Physical Review Research* **5**, 043208 (2023).
- [38] C. M. Langlett, Z.-C. Yang, J. Wildeboer, A. V. Gorshkov, T. Iadecola, and S. Xu, Rainbow scars: From area to volume law, *Physical Review B* **105**, L060301 (2022).
- [39] A. Pizzi, B. Evrard, C. B. Dag, and J. Knolle, Quantum scars in many-body systems, arXiv preprint arXiv:2408.10301 (2024).
- [40] M. C. Bañuls *et al.*, Simulating Lattice Gauge Theories within Quantum Technologies, *Eur. Phys. J. D* **74**, 165 (2020), arXiv:1911.00003 [quant-ph].
- [41] N. Klco, A. Roggero, and M. J. Savage, Standard model physics and the digital quantum revolution: thoughts about the interface, *Rept. Prog. Phys.* **85**, 064301 (2022), arXiv:2107.04769 [quant-ph].
- [42] C. W. Bauer, Z. Davoudi, A. B. Balantekin, T. Bhattacharya, M. Carena, W. A. De Jong, P. Draper, A. El-Khadra, N. Gemelke, M. Hanada, *et al.*, Quantum simulation for high-energy physics, *PRX quantum* **4**, 027001 (2023).
- [43] D. Beck, J. Carlson, Z. Davoudi, J. Formaggio, S. Quaglioni, M. Savage, J. Barata, T. Bhattacharya, M. Bishof, I. Cloet, *et al.*, Quantum information science and technology for nuclear physics. input into us long-range planning, 2023, arXiv preprint arXiv:2303.00113 (2023).
- [44] C. W. Bauer, Z. Davoudi, N. Klco, and M. J. Savage, Quantum simulation of fundamental particles and forces, *Nature Reviews Physics* **5**, 420 (2023).
- [45] N. Mueller, T. V. Zache, and R. Ott, Thermalization of gauge theories from their entanglement spectrum, *Physical Review Letters* **129**, 011601 (2022).
- [46] Z.-Y. Zhou, G.-X. Su, J. C. Halimeh, R. Ott, H. Sun, P. Hauke, B. Yang, Z.-S. Yuan, J. Berges, and J.-W. Pan, Thermalization dynamics of a gauge theory on a quantum simulator, *Science* **377**, 311 (2022).
- [47] L. Ebner, A. Schäfer, C. Seidl, B. Müller, and X. Yao, Eigenstate thermalization in  $(2+1)$ -dimensional  $su(2)$  lattice gauge theory, *Physical Review D* **109**, 014504 (2024).
- [48] N. Mueller, T. Wang, O. Katz, Z. Davoudi, and M. Cetina, Quantum computing universal thermalization dynamics in a  $(2+1)$  d lattice gauge theory, arXiv preprint arXiv:2408.00069 (2024).
- [49] E. Fradkin, *Field theories of condensed matter physics* (Cambridge University Press, 2013).
- [50] H. Kleinert, *Gauge Fields in Condensed Matter: Vol. 1: Superflow and Vortex Lines (Disorder Fields, Phase Transitions) Vol. 2: Stresses and Defects (Differential Geometry, Crystal Melting)* (World Scientific, 1989).
- [51] S. Das Sarma, M. Freedman, and C. Nayak, Topological quantum computation, *Physics Today* **59**, 32 (2006).
- [52] C. Nayak, S. H. Simon, A. Stern, M. Freedman, and S. Das Sarma, Non-abelian anyons and topological quantum computation, *Rev. Mod. Phys.* **80**, 1083 (2008).
- [53] V. Lahtinen and J. K. Pachos, A Short Introduction to Topological Quantum Computation, *SciPost Phys.* **3**, 021 (2017).
- [54] D. Gottesman, The heisenberg representation of quantum computers, arXiv preprint quant-ph/9807006 (1998).
- [55] S. Aaronson and D. Gottesman, Improved simulation of stabilizer circuits, *Physical Review A—Atomic, Molecular, and Optical Physics* **70**, 052328 (2004).
- [56] S. Bravyi and A. Kitaev, Universal quantum computation with ideal clifford gates and noisy ancillas, *Physical Review A—Atomic, Molecular, and Optical Physics* **71**, 022316 (2005).
- [57] E. T. Campbell, B. M. Terhal, and C. Vuillot, Roads towards fault-tolerant universal quantum computation, *Nature* **549**, 172 (2017).
- [58] Supplemental Material at [URL will be inserted by publisher] which contains details about the symmetry structure of the model, the analytic derivation of the QMBS solutions and further details, and details of the experimental proposal, which includes [65–67, 69, 83–92].
- [59] By fixing the superselection sector,  $\alpha$  and  $\beta$ , we create a state with a defect localized either inside or outside of  $A$ . A superposition with defect trapped *outside* of  $A$  would have all  $X_p X_{p+L}$  and  $Z_p Z_{p+L}$  identical everywhere *inside* of  $A$ .
- [60] S. Moudgalya and O. I. Motrunich, Hilbert space fragmentation and commutant algebras, *Physical Review X* **12**, 10.1103/physrevx.12.011050 (2022).
- [61] S. Moudgalya and O. I. Motrunich, *Exhaustive characterization of quantum many-body scars using commutant algebras* (2023), arXiv:2209.03377 [cond-mat.str-el].
- [62] S. Moudgalya and O. I. Motrunich, From symmetries to commutant algebras in standard hamiltonians, *Annals of Physics* **455**, 169384 (2023).
- [63] B. van Voorden, J. c. v. Minář, and K. Schoutens, Quantum many-body scars in transverse field ising ladders and beyond, *Phys. Rev. B* **101**, 220305 (2020).
- [64] This space is, roughly, the space spanned by eigenstates in the window  $E \pm \Delta E/2$ , where  $E = \langle H \rangle$  and  $\Delta E^2 \equiv \langle H^2 \rangle - \langle H \rangle^2$ , and  $\langle \cdot \rangle$  the initial state expectation value.
- [65] R. Somma, G. Ortiz, J. E. Gubernatis, E. Knill, and R. Laflamme, Simulating physical phenomena by quantum networks, *Physical Review A* **65**, 042323 (2002).
- [66] M. Knapp, A. Kantian, T. Giamarchi, I. Bloch, M. D.

- Lukin, and E. Demler, Probing real-space and time-resolved correlation functions with many-body ramsay interferometry, *Physical review letters* **111**, 147205 (2013).
- [67] N. Mueller, J. A. Carolan, A. Connelly, Z. Davoudi, E. F. Dumitrescu, and K. Yeter-Aydeniz, Quantum computation of dynamical quantum phase transitions and entanglement tomography in a lattice gauge theory, *PRX Quantum* **4**, 030323 (2023).
- [68] A. Elben, S. T. Flammia, H.-Y. Huang, R. Kueng, J. Preskill, B. Vermersch, and P. Zoller, The randomized measurement toolbox, *Nat. Rev. Phys.* **5**, 9 (2023).
- [69] J. Bringewatt, J. Kunjummen, and N. Mueller, Randomized measurement protocols for lattice gauge theories, *Quantum* **8**, 1300 (2024).
- [70] C. Kokail, R. van Bijnen, A. Elben, B. Vermersch, and P. Zoller, Entanglement hamiltonian tomography in quantum simulation, *Nat. Phys.* **17**, 936 (2021).
- [71] C. Kokail, B. Sundar, T. V. Zache, A. Elben, B. Vermersch, M. Dalmonte, R. van Bijnen, and P. Zoller, Quantum variational learning of the entanglement hamiltonian, *Phys. Rev. Lett.* **127**, 170501 (2021).
- [72] Z.-W. Liu and A. Winter, Many-body quantum magic, *PRX Quantum* **3**, 020333 (2022).
- [73] P. S. Tarabunga, E. Tirrito, T. Chanda, and M. Dalmonte, Many-body magic via pauli-markov chains—from criticality to gauge theories, *PRX Quantum* **4**, 040317 (2023).
- [74] D. Rattacaso, L. Leone, S. F. Oliviero, and A. Hamma, Stabilizer entropy dynamics after a quantum quench, *Physical Review A* **108**, 042407 (2023).
- [75] A. Catalano, J. Odavić, G. Torre, A. Hamma, F. Franchini, and S. Giampaolo, Magic phase transition and non-local complexity in generalized  $w$  state, arXiv preprint arXiv:2406.19457 (2024).
- [76] C. E. Robin and M. J. Savage, The magic in nuclear and hypernuclear forces, arXiv preprint arXiv:2405.10268 (2024).
- [77] F. Bröckemeier, S. M. Hengstenberg, J. W. Keeble, C. E. Robin, F. Rocco, and M. J. Savage, Quantum magic and multi-partite entanglement in the structure of nuclei, arXiv preprint arXiv:2409.12064 (2024).
- [78] I. Chernyshev, C. E. Robin, and M. J. Savage, Quantum magic and computational complexity in the neutrino sector, arXiv preprint arXiv:2411.04203 (2024).
- [79] L. Leone, S. F. Oliviero, and A. Hamma, Stabilizer rényi entropy, *Physical Review Letters* **128**, 050402 (2022).
- [80] R. Smith, Z. Papić, and A. Hallam, Non-stabilizerness in kinetically-constrained rydberg atom arrays, arXiv preprint arXiv:2406.14348 (2024).
- [81] X. Turkeshi, A. Dymarsky, and P. Sierant, Pauli spectrum and magic of typical quantum many-body states, arXiv preprint arXiv:2312.11631 (2023).
- [82] Our argument is based solely on the observation in [79] that, for a spin-1/2 (qubits) system, the  $\alpha$ -SRE is bounded by  $\log(d)$  (specifically, it is bounded by  $\log(d+1) - \log(2)$  for  $\alpha = 2$ ), where  $d(=4L)$  is the dimension of the space. Although the scar subspace is not merely a system of qubits and the assumptions of [79] do not directly apply, we would find a different scaling with  $L$  surprising.
- [83] Scholarpedia [http://www.scholarpedia.org/article/Loschmidt\\_echo](http://www.scholarpedia.org/article/Loschmidt_echo) (Oct 31, 2024).
- [84] J. M. Pino, J. M. Dreiling, C. Figgatt, J. P. Gaebler, S. A. Moses, M. Allman, C. Baldwin, M. Foss-Feig, D. Hayes, K. Mayer, *et al.*, Demonstration of the trapped-ion quantum ccd computer architecture, *Nature* **592**, 209 (2021).
- [85] K. Rudinger, G. J. Ribeill, L. C. Govia, M. Ware, E. Nielsen, K. Young, T. A. Ohki, R. Blume-Kohout, and T. Proctor, Characterizing midcircuit measurements on a superconducting qubit using gate set tomography, *Physical Review Applied* **17**, 014014 (2022).
- [86] IBM, How to measure and reset a qubit in the middle of a circuit execution, <https://www.ibm.com/quantum/blog/quantum-mid-circuit-measurement>.
- [87] L. Botelho, A. Glos, A. Kundu, J. A. Miszczak, Ö. Salehi, and Z. Zimborás, Error mitigation for variational quantum algorithms through mid-circuit measurements, *Physical Review A* **105**, 022441 (2022).
- [88] H. J. Briegel, D. E. Browne, W. Dür, R. Raussendorf, and M. Van den Nest, Measurement-based quantum computation, *Nature Physics* **5**, 19 (2009).
- [89] M. Aguado, G. Brennen, F. Verstraete, and J. I. Cirac, Creation, manipulation, and detection of abelian and non-abelian anyons in optical lattices, *Physical review letters* **101**, 260501 (2008).
- [90] N. Tantivasadakarn, R. Thorngren, A. Vishwanath, and R. Verresen, Long-range entanglement from measuring symmetry-protected topological phases, *Physical Review X* **14**, 021040 (2024).
- [91] E. Bäumer and S. Woerner, Measurement-based long-range entangling gates in constant depth, arXiv preprint arXiv:2408.03064 (2024).
- [92] A. Angrisani, A. Schmidhuber, M. S. Rudolph, M. Cerezo, Z. Holmes, and H.-Y. Huang, Classically estimating observables of noiseless quantum circuits, arXiv preprint arXiv:2409.01706 (2024).

## SUPPLEMENTAL MATERIAL

### A. Entanglement Structure and Symmetries

In this subsection, we provide additional discussion of the symmetries and entanglement structure of the LGT model and its Ising dual. The (2+1)d  $\mathbb{Z}_2$  LGT with periodic boundary conditions exhibits several symmetries, including local Gauss laws,

$$G_s \equiv \prod_{\nu \in s} \sigma_\nu^z \quad (13)$$

at each site or ‘vertex’  $s$ , as shown in Fig. 5(a). Since  $\prod_s G_s = 1$ , these operators define  $2^{2L-1}$  distinct superselection sectors of the model. We focus on the sector where  $G_s = 1$  for all  $s$ , commonly referred to as the ‘physical sector’. Additionally, there are two ribbon operators, depicted in Fig. 5(b),

$$V_{x,y} \equiv \prod_{\nu \in \mathcal{L}_{x/y}} \sigma_\nu^z, \quad (14)$$

which wind non-trivially around the two periodic directions of the lattice and commute with the Hamiltonian, i.e.,  $[H, V_x] = [H, V_y] = 0$ . These symmetries result in



a total of  $2^{2L+1}$  superselection sectors. If a state is an eigenstate of these operators—meaning it is not a superposition of different sectors—then any bipartition into a subsystem  $A$  and its complement  $\bar{A}$ ,

$$\rho_A \equiv \text{Tr}_{\bar{A}}(\rho), \quad (15)$$

will inherit a specific symmetry structure, as discussed in the main text. The remnant of a Gauss operator, shown in Fig. 2(b) of the main text, that consists of three of four legs of the Gauss law operator that are inside  $A$ , at a boundary site  $s'$  (i.e.  $s'$  is the site just beyond the plaquette  $a$  or just before plaquette  $b$ ) is denoted by

$$\prod_{\nu \sim s'} \sigma_\nu^z = \sigma_{\nu_{1/2}^{a/b}}^z, \quad (16)$$

where  $\nu \sim s'$  means that only operators within  $A$  are included in the product. In the equality,  $\nu_{1/2}^{a/b}$  refers to one of horizontal links just outside of the subsystem, just as shown in Fig. 2(b), the identity is just a reorganization of Gauss law,  $G_s = 1$ . The argument made in the main text, that any superposition of scar basis states in the LGT for odd  $L$  have zero distillable entanglement, is based on  $\sigma_\nu^z$ , where  $\nu'$  is either of the horizontal links  $\nu_{1/2}^{a/b}$  in Fig. 2(b), and thus  $\prod_{\nu \in s'} \sigma_\nu^z$  labeling superselection sectors.

To illustrate better that these (four) operators label symmetry sectors, note that they commute with  $\rho_A$ ,

$$\left[ \prod_{\nu \sim s'} \sigma_\nu^z, \rho_A \right] = \left[ \sigma_{\nu_{1/2}^{a/b}}^z, \rho_A \right] = 0, \quad (17)$$

and can thus be simultaneously diagonalized, defining symmetry blocks. This can be understood as follows:  $\rho_A$  can be expressed as a sum of Pauli strings within  $A$ ,

$$\rho_A = \frac{1}{2^{d_A}} \sum_{O \in P_A} \langle O \rangle O, \quad (18)$$

where  $P_A$  are all Pauli strings with non-zero expectation value within  $A$ , and  $d_A$  is the number of spins in  $A$ . Any of the four operators on the l.h.s of Eq. (16) may be part of this sum and may have a non-zero expectation value. However, no other operator in  $A$  fails to commute with it because it is identical, by means of Gauss law, to the r.h.s of Eq. (16), an operator clearly outside of  $A$ . Thus  $\rho_A$  commutes with it, marking superselection sectors.

The same applies to the ribbon operator shown in Fig. 2(c), defined as  $V_x^A = \prod_{\nu \sim \mathcal{L}_x^A}$ , where  $\mathcal{L}_x^A = \mathcal{L}_x \cap A$ . Since  $V_x = V_x^A V_x^{\bar{A}}$ , with  $V_x^{\bar{A}}$  being the analogous ribbon operator in the complement of  $A$ , the fixed value of  $V_x$  implies, by a similar argument, that  $V_x^A$  defines a symmetry sector of  $\rho_A$ . For the other ribbon  $V_y$ , note that, since the lattice is bipartitioned along  $y$ , it remains a symmetry operator for both the global state and  $\rho_A$ ; however, as it equals the product of two Gauss laws along  $y$ , it does not define an independent symmetry block. Although there are six symmetry operators in total (four

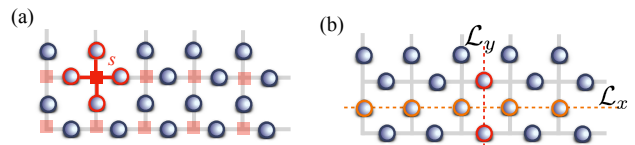


FIG. 5. *Symmetries of the LGT.* (a) Shown are  $2L$  Gauss laws, Eq. (13), at sites  $s$ , which are local symmetry operators that commute with the Hamiltonian  $H$ , thereby defining superselection sectors. (b) For periodic boundary conditions, the ribbon operators  $V_x$  and  $V_y$ , Eq. (14), defined along  $\mathcal{L}_x$  and  $\mathcal{L}_y$ , respectively, specify additional superselection sectors.

Gauss laws and two ribbons), only three of them are independent, leading to  $2^3 = 8$  non-zero symmetry blocks.

The entanglement structure of the dual Ising model is fundamentally different from that of the LGT, even though both predict identical expectation values for any operator when mapped between the two formulations. The dual formulation possesses only one symmetry: parity,

$$P_X = \prod_{p=1}^{2L} X_p = 1 \quad (19)$$

which corresponds to the requirement that the product of all plaquettes equals one in the LGT, a condition necessary for the LGT-to-Ising mapping under periodic boundary conditions. This induces a two-block symmetry structure in the reduced density matrix describing any bipartition in the Ising dual. As with the LGT, the parity of  $A$ ,  $P_X^A = \prod_{p \in A} X_p$  is a symmetry of  $\rho_A$ , thereby defining the symmetry blocks: To maintain  $P_X = 1$  parity globally, the subsystem can have either even or odd  $X$ -parity, or be in any superposition thereof.

Given the specific entanglement structure arising from the symmetries of a subsystem in either formulation, it is natural to decompose the von Neumann entanglement entropy into two components: the ‘symmetry’ component,  $S^{\text{symm.}}$ , and the ‘distillable’ component,  $S^{\text{dist.}}$ , as defined in Eq. (7). Given the number of symmetry sectors, the symmetry entanglement can be at most  $\log(2)$  in the Ising formulation, and  $3 \log(2)$  in the LGT. As discussed in the main text and further elaborated below, the scar states in the LGT exhibit zero distillable entanglement (for even and odd  $L$ ) but possess non-zero symmetry entanglement. This characteristic is important: without separating the von Neumann entropy into these components, distinguishing scar states from non-scar states and revealing their stabilizer origin would have been impossible.

## B. Derivation of the Scar Solutions

The  $\mathbb{Z}_2$  LGT model with periodic boundary conditions, Eq. (1) of the main text, can be mapped onto a two-leg

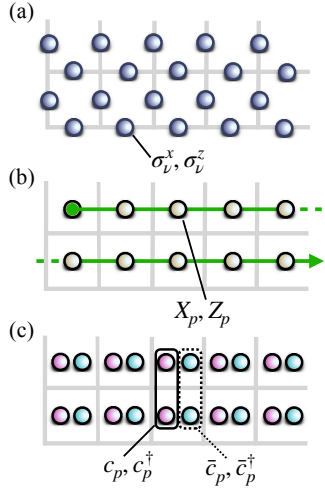


FIG. 6. *Analytic Derivation.* (a) The derivation of the scar eigenstates presented in this Letter begins with the degrees of freedom in the  $\mathbb{Z}_2$  lattice gauge theory (LGT), represented by spins located on the links of a  $L \times 2$ -site lattice with periodic boundary conditions. (b) This system is then mapped onto a dual Ising model, subject to the parity constraint  $\prod_p X_p = 1$ , where spin-1/2 degrees of freedom reside at the centers of the plaquettes (denoted by  $p = 1, \dots, 2L$ ). A Jordan-Wigner transformation (indicated by the green arrow) initiates in the top row (covering plaquettes  $1, \dots, L$ ) and extends to the bottom row (from sites  $L+1$  to  $2L$ ), transforming the system into a two-component Majorana representation. (c) The Majorana modes are combined vertically to form a two-flavor fermion representation, where  $p = 1, \dots, L$  denotes one-dimensional sites. This representation enables the identification of scar subspaces for both even and odd  $L$  via the commutant of the algebra generated by the terms in  $H$ .

transverse field Ising model (TFI<sup>2</sup>), Eq. (2) of the main text, under the constraint  $\prod_p X_p = 1$  which ensures that the product of all plaquettes is one, an identity on the LGT side, see Fig. 6(a) and (b). The TFI<sup>2</sup> is mapped onto a fermionic system via a Jordan-Wigner transformation that runs from the first spin in the top row to the last spin in the top row, then continuing at the first spin on the bottom row and ending at the last spin in the bottom row, see Fig. 6(b). As shown in Fig. 6(c), this is written in terms of Majorana operators,  $\gamma_p, \bar{\gamma}_p$ ,  $p = 1, \dots, 2L$  with  $\gamma_p^2 = \bar{\gamma}_p^2 = 1$  and  $\{\gamma_p, \gamma_q\} = \{\bar{\gamma}_p, \bar{\gamma}_q\} = 2\delta_{pq}$ ,  $\{\gamma_p, \bar{\gamma}_q\} = 0$ , as follows

$$X_p = -i\gamma_p\bar{\gamma}_p, \quad Z_p = \prod_{q=1}^{p-1} (i\gamma_q\bar{\gamma}_q)\gamma_p. \quad (20)$$

Next, we define two species fermionic operators by combining the Majorana modes *vertically along y*, i.e.,

$$\begin{aligned} c_p &= \frac{1}{2}(\gamma_p - i\gamma_{p+L}), & \bar{c}_p &= \frac{1}{2}(\bar{\gamma}_p - i\bar{\gamma}_{p+L}), \\ c_p^\dagger &= \frac{1}{2}(\gamma_p + i\gamma_{p+L}), & \bar{c}_p^\dagger &= \frac{1}{2}(\bar{\gamma}_p + i\bar{\gamma}_{p+L}). \end{aligned} \quad (21)$$

The fermion parity operators are given as

$$(-1)^{c_p^\dagger c_p} = i\gamma_p\gamma_{p+L}, \quad (-1)^{\bar{c}_p^\dagger \bar{c}_p} = i\bar{\gamma}_p\bar{\gamma}_{p+L}, \quad (22)$$

so that

$$X_p X_{p+L} \equiv -(-1)^{c_p^\dagger \bar{c}_p + \bar{c}_p^\dagger c_p}, \quad (23)$$

marks the combined-species fermion parity. We define the vacuum state by requiring  $c_p|0\rangle = \bar{c}_p|0\rangle = 0$  for all  $p$ , with the mode ordering from left to right in ascending order, i.e.,  $c_1^\dagger \bar{c}_1^\dagger \dots c_L^\dagger \bar{c}_L^\dagger |0\rangle$ . Note that the constraint

$$1 = \prod_{p=1}^{2L} X_p = \prod_{p=1}^L X_p X_{p+L} = (-1)^L \prod_{p=1}^L (-1)^{c_p^\dagger c_p + \bar{c}_p^\dagger \bar{c}_p}, \quad (24)$$

either represents the fermion parity for even  $L$  or the *negative* fermion parity for odd  $L$ . Consequently, for even  $L$ , only an even number of fermion or hole excitations are allowed, whereas for odd  $L$ , only an odd number of fermion or hole excitations are possible. This property is crucial for the scar solutions.

In this representation, two of the three terms of the Ising Hamiltonian, Eq. (2), conserve the total fermion number,

$$\hat{N} = \sum_{p=1}^L (c_p^\dagger c_p + \bar{c}_p^\dagger \bar{c}_p), \quad (25)$$

which ranges from  $\hat{N} = 0$  to  $\hat{N} = 2L$ . Concretely, using Eqs. (20-21), we can rewrite the first term in Eq. (2) as

$$\begin{aligned} X_p + X_{p+L} &= i\bar{\gamma}_p\gamma_p + i\bar{\gamma}_{p+L}\gamma_{p+L} \\ &= 2i(\bar{c}_p c_p^\dagger + \bar{c}_p^\dagger c_p). \end{aligned} \quad (26)$$

A similar derivation for the third term, for  $p < L$ , yields

$$\begin{aligned} Z_p Z_{p+1} + Z_{p+L} Z_{p+L+1} &= i\bar{\gamma}_p\gamma_{p+1} + i\bar{\gamma}_{p+L}\gamma_{p+L+1} \\ &= 2i(\bar{c}_p c_{p+1}^\dagger + \bar{c}_p^\dagger c_{p+1}), \end{aligned} \quad (27)$$

demonstrating that both terms conserve particle number. For  $p = L$ , however, we find

$$Z_1 Z_L + Z_{L+1} Z_{2L} = \prod_{q=1}^L (i\gamma_q\bar{\gamma}_q) (i\gamma_1\bar{\gamma}_L + i\gamma_{L+1}\bar{\gamma}_{2L}) \quad (28)$$

where  $i\gamma_1\bar{\gamma}_L + i\gamma_{L+1}\bar{\gamma}_{2L} = 2i(c_1^\dagger \bar{c}_L + c_1 \bar{c}_L^\dagger)$  conserves particle number, but the string  $\prod_{q=1}^L (i\gamma_q\bar{\gamma}_q)$  does not. This string arises because  $Z_1 Z_L + Z_{L+1} Z_{2L}$  is a non-local operator connecting across the periodic boundary condition, reflecting the choice of Jordan-Wigner map between spins and fermions shown in Fig. 6(b). Similarly, the remaining term in Eq. (2) also involves also a Jordan-Wigner string:

$$Z_p Z_{p+L} = i \prod_{q=0}^{L-1} (i\gamma_{p+q}\bar{\gamma}_{p+q}) i\gamma_p\gamma_{p+L} \quad (29)$$

which does not conserve fermion number either.

Despite not conserving particle number, both Eq. (28) and Eq. (29) exhibit particle-hole symmetry, i.e., conjugating  $\hat{N}$  to  $2L - \hat{N}$  and vice versa. Consequently, all terms in the Hamiltonian conserve  $(\hat{N} - L)^2$ . As we will show below, the scar solutions are to be found, for even  $L$ , in the  $(\hat{N} - L)^2 = L^2$  subspace, corresponding to the completely empty,  $\hat{N} = 0$ , or fully filled,  $\hat{N} = 2L$ , states. For odd  $L$ , the scars lie in the  $(\hat{N} - L)^2 = (1 - L)^2 = (2L - 1 - L)^2$  subspace, i.e., the combined single-particle,  $\hat{N} = 1$ , and single-hole,  $\hat{N} = 2L - 1$ , states.

Equipped with this, we will now explicitly demonstrate that Eq. (2) posses exact scar eigenstates for even  $L$  which are the Fock vacuum and the fully occupied states, and furthermore that for odd  $L$  the scar subspace is spanned by  $4L$  single-particle and single-hole excitations of the  $\bar{c}^\dagger$  and  $c^\dagger$  modes,  $H^{\text{dual}}$  has no matrix elements connecting these to any other state.

### 1. Scar Solutions for even $L$

Given the properties discussed in the previous section, we posit that the two scar solutions for even  $L$  are found in the smallest eigenspaces of  $(\hat{N} - L)^2$ : the vacuum state  $|0\rangle$  and the fully occupied state

$$|\Lambda\rangle \equiv \prod_p c_p^\dagger \bar{c}_p^\dagger |0\rangle \quad (30)$$

where the product is in ascending order. These are eigenstates with eigenvalue zero of all terms in Eq. (2), and by extension of Eq. (1), which we will show now. Both  $|0\rangle$  and  $|\Lambda\rangle$  are uniquely specified via the fermion parity, specifically for these states

$$1 = (-1)^{c_p^\dagger c_p + \bar{c}_p^\dagger \bar{c}_p} = -X_p X_{p+L}, \quad (31)$$

where we used Eq. (23), and

$$\begin{aligned} 1 &= (-1)^{\bar{c}_p^\dagger \bar{c}_p + c_{p+1}^\dagger c_{p+1}} = \bar{\gamma}_p \gamma_{p+1} \bar{\gamma}_{p+L} \gamma_{p+L+1} \\ &= -Z_p Z_{p+1} Z_{p+L} Z_{p+L+1}, \end{aligned} \quad (32)$$

where in the last equality we have used that  $\gamma_p \equiv \prod_{k=1}^{p-1} (-X_k) Z_p$  and  $\bar{\gamma}_p \equiv -i X_p \prod_{k=1}^{p-1} (-X_k) Z_p$ . From Eq. (31) it follows that the space spanned by  $|0\rangle$  and  $|\Lambda\rangle$  must have  $X_p X_{p+L} = -1$  and from Eq. (32) that  $Z_p Z_{p+L} = -Z_{p+1} Z_{p+L+1}$  for all  $p$ . We can thus pick the two states given in Eq. (3) of the main text to span the even- $L$  subspace.

We will show now that these are *exact* eigenstates with eigenvalue zero for any value of the coupling  $g$ . Specifically,  $\rho_{1/2}$  are eigenstates of, i.e. commutes with, every individual term in Eq. (3). We write  $H^{\text{dual}} \equiv$

$H_A + H_B + H_C$  where

$$H_A \equiv - \sum_{p=1}^L [X_p + X_{p+L}], \quad (33)$$

$$H_B \equiv -\tilde{g} \sum_{p=1}^L Z_p Z_{p+L}, \quad (34)$$

$$H_C \equiv - \sum_{p=1}^L g_p [Z_p Z_{p+1} + Z_{p+L} Z_{p+L+1}]. \quad (35)$$

First note that if  $X_p X_{p+L} = -1$  (Eq. (31)), then  $X_p = -X_{p+L}$ , and therefore  $H_A |\Psi_{1/2}\rangle = 0$  (or alternatively  $[H_A, \rho_{1/2}] = 0$ ). Furthermore, from Eq. (32) it also follows that

$$Z_p Z_{p+1} = -Z_{p+L} Z_{p+L+1} \quad (36)$$

and thus  $H_C |\Psi_{1/2}\rangle = 0$ . Finally, note that

$$H_B |\psi_{1/2}\rangle = -\tilde{g} \sum_{p=1}^L \pm (-1)^p |\psi_{1/2}\rangle = 0, \quad (37)$$

because  $L$  is even. Therefore  $|\psi_{1/2}\rangle$  are degenerate exact eigenstates of  $H^{\text{dual}}$  with eigenvalue zero (and thus of Eq. (1) on the other side of the duality). Because the states  $|\psi_{1/2}\rangle$ , as well as  $|0\rangle$  and  $|\Lambda\rangle$ , are product states, their von Neumann entanglement entropy is zero for any bipartition. More specifically, separate symmetry and distillable entanglement components can be defined via Eq. (7). Both the distillable and the symmetry component are zero,  $S_{\text{dist}}^{\text{dual}} = S_{\text{sym}}^{\text{dual}} = 0$ , for the even- $L$  scars in the Ising formulation. In the LGT formulation the distillable entanglement is also zero,  $S_{\text{dist}}^{\text{LGT}} = 0$ , but the scars are not product states. A non-zero symmetry components stems from the Gauss laws at the boundary separating a subsystem from its complement, see the discussion in Section A.

### 2. Scar Subspace for odd $L$

For odd  $L$ , we now discuss a subspace spanned by scar states. The states  $|0\rangle$  and  $|\Lambda\rangle$  are not allowed for odd  $L$  because of Eq. (23), instead only states with an odd fermion-parity are permitted. We posit that the scar subspace is spanned by the following  $4L$  single-particle and single-hole states,

$$|\psi_p\rangle \equiv c_p^\dagger |0\rangle, \quad |\bar{\psi}_p\rangle \equiv \bar{c}_p^\dagger |0\rangle, \quad (38)$$

$$|\chi_p\rangle \equiv c_p |\Lambda\rangle, \quad |\bar{\chi}_p\rangle \equiv -\bar{c}_p |\Lambda\rangle, \quad (39)$$

$|\Lambda\rangle$  is defined in Eq. (30) and the fermion-parity is consistent with Eq. (23) for odd  $L$ . The terms in the Hamiltonian can be written in terms of Majorana operators and, subsequently, via fermion Fock operators. The plaquette

term is

$$H_A = - \sum_{p=1}^L (i\bar{\gamma}_p \gamma_p + i\bar{\gamma}_{p+L} \gamma_{p+L}) = -2i \sum_{p=1}^L (\bar{c}_p^\dagger c_p - c_p^\dagger \bar{c}_p), \quad (40)$$

which conserves the total fermion number, Eq. (25). The electric terms in the Hamiltonian can be written as

$$H_B = \tilde{g} \sum_{p=1}^L \prod_{q=0}^{L-1} (i\gamma_{p+q} \bar{\gamma}_{p+q}) \gamma_p \gamma_{p+L} \quad (41)$$

and

$$H_C = -g \sum_{p=1}^{L-1} (i\bar{\gamma}_p \gamma_{p+1} + i\bar{\gamma}_{p+L} \gamma_{p+L+1}) - gV_x \prod_{q=1}^L (i\gamma_q \bar{\gamma}_q) (i\gamma_1 \bar{\gamma}_L + i\gamma_{L+1} \bar{\gamma}_{2L}) \quad (42)$$

whose properties are more difficult to discern. To understand the action of  $H_3$  (Eq. (42)) note that

$$i\bar{\gamma}_p \gamma_{p+1} + i\bar{\gamma}_{p+1} \gamma_p = 2i(\bar{c}_p^\dagger c_{p+1} - c_{p+1}^\dagger \bar{c}_p), \quad (43)$$

$$i\gamma_1 \bar{\gamma}_L + i\gamma_{L+1} \bar{\gamma}_{2L} = 2i(c_1^\dagger \bar{c}_L - \bar{c}_p^\dagger c_1), \quad (44)$$

are particle number conserving terms. Importantly, the product in the second line of Eq. (42) can be written as

$$\prod_{q=1}^L (i\gamma_q \bar{\gamma}_q) = \prod_{q=1}^L i(c_q^\dagger \bar{c}_q^\dagger + c_q^\dagger \bar{c}_q + c_q \bar{c}_q^\dagger + c_q \bar{c}_q) \quad (45)$$

and it conserves the space spanned by Eqs. (38-39). Specifically, one can show that

$$\begin{aligned} \prod_{q=1}^L (i\gamma_q \bar{\gamma}_q) |\psi_p\rangle &= -i^L |\chi_p\rangle, \\ \prod_{q=1}^L (i\gamma_q \bar{\gamma}_q) |\bar{\psi}_p\rangle &= i^L |\bar{\chi}_p\rangle, \\ \prod_{q=1}^L (i\gamma_q \bar{\gamma}_q) |\chi_p\rangle &= i^L |\psi_p\rangle, \\ \prod_{q=1}^L (i\gamma_q \bar{\gamma}_q) |\bar{\chi}_p\rangle &= -i^L |\bar{\psi}_p\rangle. \end{aligned} \quad (46)$$

Moreover, for Eq. (41), one finds that  $\gamma_p \gamma_{p+L} = 2ic_p^\dagger c_p$  and that

$$\begin{aligned} \prod_{q=0}^{L-1} (i\gamma_{p+q} \bar{\gamma}_{p+q}) |\psi_p\rangle &= i^L (-1)^p \theta(k, q) |\chi_p\rangle, \\ \prod_{q=0}^{L-1} (i\gamma_{p+q} \bar{\gamma}_{p+q}) |\bar{\psi}_k\rangle &= -i^L (-1)^p \theta(k, q) |\bar{\chi}_k\rangle, \\ \prod_{q=0}^{L-1} (i\gamma_{p+q} \bar{\gamma}_{p+q}) |\chi_k\rangle &= -i^L (-1)^p \theta(k, q) |\psi_k\rangle, \\ \prod_{q=0}^{L-1} (i\gamma_{p+q} \bar{\gamma}_{p+q}) |\bar{\chi}_k\rangle &= i^L (-1)^p \theta(k, q) |\bar{\psi}_k\rangle, \end{aligned} \quad (47)$$

where  $\theta(k, q) \equiv 1$  if  $k \leq q$  and  $-1$  otherwise. This establishes that  $H^{\text{dual}}$  (and thus  $H$ ) has no matrix elements between the scar and non-scar subspaces.

While a rather lengthy derivation brought these results, a more elegant solution can be found noting that Eqs. (38-39) are uniquely specified by

$$(-1)^{c_k^\dagger c_k + \bar{c}_k^\dagger \bar{c}_k} = \begin{cases} 1 & \text{if } k = p \\ -1 & \text{otherwise} \end{cases}, \quad (48)$$

specifying the values of  $X_p X_{p+L}$ , and

$$(-1)^{\bar{c}_p^\dagger \bar{c}_p + c_{p+1}^\dagger c_{p+1}} = \begin{cases} -1 & \text{if } k = p \text{ or } k = p-1 \\ 1 & \text{otherwise} \end{cases} \quad (49)$$

specifying the values of  $Z_p Z_{p+L}$ . The  $4L$  states obeying Eqs. (48-49) are given in Eq. (5) of the main text. We will now work out the matrix elements of the Hamiltonian in these states. To do so, we first write them as

$$|\varphi_\alpha(k)\rangle \equiv \prod_{q \neq k} \left[ \frac{1 - X_q X_{q+L}}{\sqrt{2}} \right] \frac{1 + X_k X_{k+L}}{\sqrt{2}} |r_\alpha(k)\rangle \quad (50)$$

where  $|r_\alpha(k)\rangle$  are  $Z$ -eigenstates that realize the desired  $Z_p Z_{p+L}$  stabilizer property (but are not  $X_p X_{p+L}$  eigenstates). Choosing a convention, where the spin in the bottom row is always up, the spin in the top row selects the  $Z_p Z_{p+L}$  eigenvalue, for instance for  $\alpha = 1$ ,

$$|r_1(k)\rangle \equiv \prod_{p < k} \left| \begin{matrix} s^{(p,k)} \\ \uparrow \end{matrix} \right\rangle \left| \begin{matrix} \downarrow \\ \uparrow \end{matrix} \right\rangle \prod_{p > k} \left| \begin{matrix} \bar{s}^{(p,k)} \\ \uparrow \end{matrix} \right\rangle, \quad (51)$$

where  $s^{(p,k)} = \uparrow$  if  $k - q$  is even and otherwise  $\downarrow$ , and  $\bar{s}^{(p,k)} = \downarrow$  if  $k - 1$  is even and otherwise  $\uparrow$ . The cases  $\alpha = 2, 3, 4$  follow directly from Eq. (5). The matrix elements of  $H^{\text{dual}}$  Eq. (2) with individual terms given in Eqs. (33-33)), and identically for the LGT Hamiltonian Eq. (1), are now easily derived. For the plaquette term,  $H_A = \sum_p (X_p + X_{p+L})$ , the scar-subspace matrix elements read

$$\begin{aligned} \langle \varphi_4(k) | H_A | \varphi_1(k) \rangle &= \langle \varphi_1(k) | H_A | \varphi_4(k) \rangle \\ &= \langle \varphi_3(k) | H_A | \varphi_2(k) \rangle = \langle \varphi_2(k) | H_A | \varphi_3(k) \rangle = 2, \end{aligned} \quad (52)$$



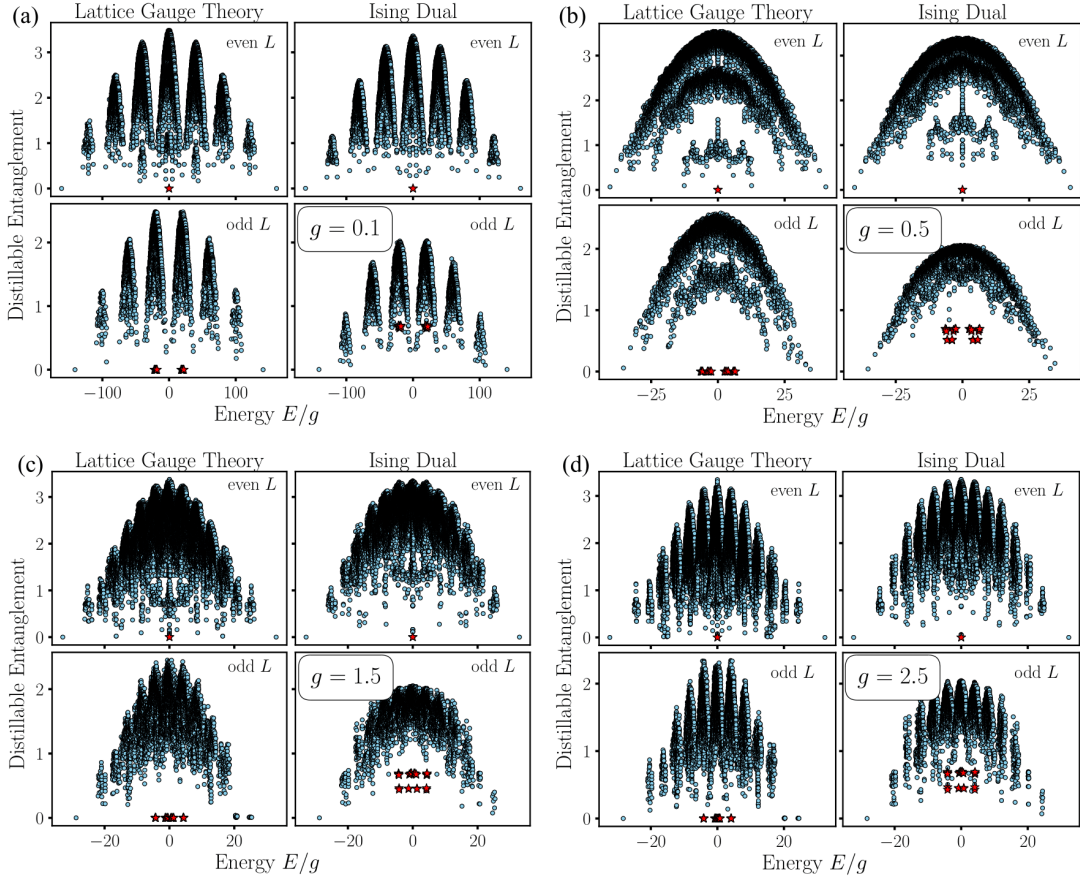


FIG. 7. *Distillable Entanglement for varying Couplings.* (a) The plot shows  $S_{\text{vN}}^{\text{dist}}$  for  $g = 0.1$ , close to the integrable point  $g = 0$ . Panels in the top row display results for an even system size  $L = 8$ , while the bottom row shows results for an odd system size  $L = 7$ . The left panels correspond to results from the LGT formulation, and the right panels to those from the Ising model. Scar states are highlighted with red stars. In the Ising dual formulation, scar states exhibit non-zero distillable entanglement, blending with other typical states and becoming indistinguishable. However, in the LGT, scar states maintain exactly zero distillable entanglement, which differentiates them clearly. (b) Results for  $g = 0.5$ . We point out a band structure visible within the typical states. This structure may be due to other (exact or approximate) protected subspaces in the model. (c)  $g = 1.5$ . (d)  $g = 2.5$ . While the limits  $g \rightarrow 0$  and  $g \rightarrow \infty$  yield ground states that are straightforward to understand, the behavior of mid-spectrum states is complex, with scar eigenstates persisting in these limits.

while the scar-subspace matrix elements of  $H_B = \sum_p Z_p Z_{p+L}$  are

$$\begin{aligned} \langle \varphi_1(k) | H_B | \varphi_1(k) \rangle &= \langle \varphi_3(k) | H_B | \varphi_3(k) \rangle = -1, \\ \langle \varphi_2(k) | H_B | \varphi_2(k) \rangle &= \langle \varphi_4(k) | H_B | \varphi_4(k) \rangle = +1. \end{aligned} \quad (53)$$

Finally, the matrix elements of  $H_C = \sum_p (Z_p Z_{p+1} + Z_{p+L} Z_{p+1+L})$  are

$$\begin{aligned} \langle \varphi_3(k-1) | H_C | \varphi_1(k) \rangle &= \langle \varphi_1(k+1) | H_C | \varphi_3(k) \rangle \\ &= \langle \varphi_4(k-1) | H_C | \varphi_2(k) \rangle = \langle \varphi_2(k+1) | H_C | \varphi_4(k) \rangle = 2. \end{aligned} \quad (54)$$

While states are represented differently in the LGT, see the main text, these matrix elements are identical between the formulations.

### C. Details of the Quantum Many-body Scar Solutions

In this section of the Supplemental Material we provide additional numerical details for the QMBS solution discussed in the main text, both in the LGT and the Ising formulation. All results are for  $V_x = V_y = 1$ , though while the  $V_y = -1$  sector is trivial, the QMBS solutions exist in all sectors.

Fig. 7 shows the distillable entanglement, for even  $L = 8$  and odd  $L = 7$ , across a range of couplings,  $g \in \{0.1, 0.5, 1.5, 2.5\}$ . The scar solutions persist for any value of the coupling and, moreover, for the LGT have exactly zero entanglement (which we verified to within machine precision). In contrast, in the Ising dual the distillable entanglement is non-zero and, depending on the coupling, the scar solutions can be indistinguishable from typical eigenstates. Notably, while the limits  $g \rightarrow 0$  and

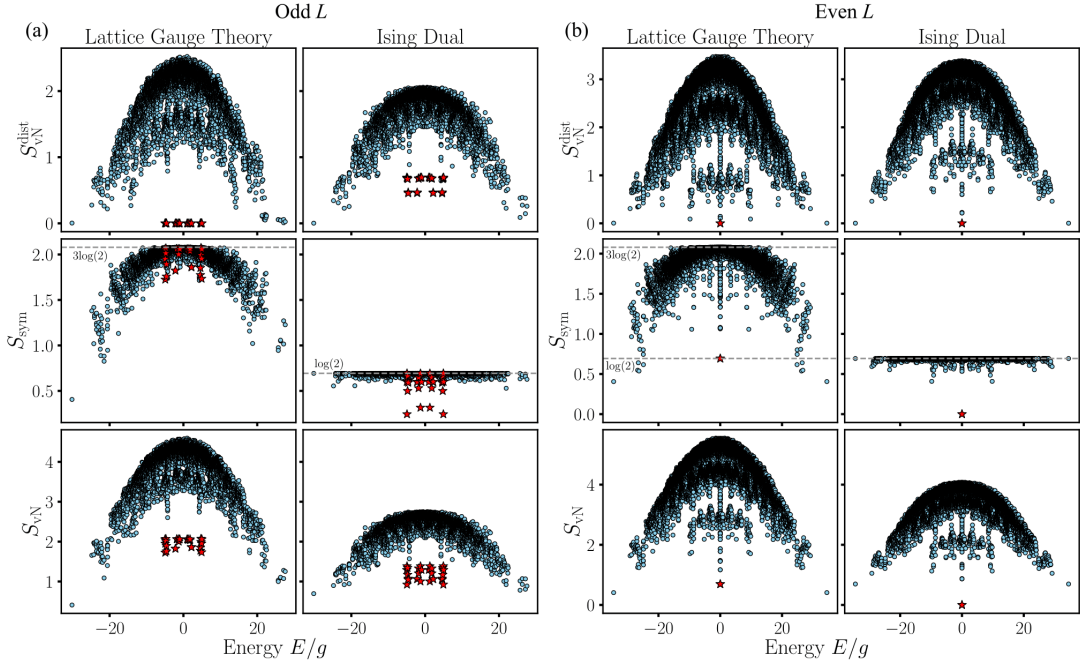


FIG. 8. *Contributions to von Neumann Entanglement Entropy.* The top row shows the distillable entanglement  $S_{\text{vN}}^{\text{dist}}$ , the middle row the symmetry entanglement  $S_{\text{vN}}^{\text{sym}} \equiv -\sum_s p_s \log(p_s)$ , and the bottom row the total von Neumann entropy  $S_{\text{vN}} = S_{\text{vN}}^{\text{dist}} + S_{\text{vN}}^{\text{sym}}$ . The left column contains results from the LGT, while the right column shows results for the Ising dual. Quantum many-body scar (QMBS) states are highlighted in red, with the maximum possible symmetry entanglement indicated by horizontal gray dashed lines. (a) Results for odd system size  $L = 7$  and (b) for even system size  $L = 8$ . For  $g = 0.9$ , these results show that QMBS states can be clearly distinguished by their distillable entanglement in the LGT, where they exhibit exactly zero values. By contrast, the total von Neumann entropy, although widely used, is finite and therefore less reliable for identifying QMBS states. Indeed, at other coupling values and in smaller systems, scar states may blend with typical states in terms of  $S_{\text{vN}}$  even within the LGT, rendering them indistinguishable.

$g \rightarrow \infty$  are well understood for the ground states of the model, mid-spectrum states behave highly non-trivial in these limits with the scar states persisting. Additionally, in Fig. 7(b) we observe an intricate band structure within the typical eigenstates. We speculate that these are due to additional protected subspaces potentially those that, in the fermionic formulation, are singled out by  $(\hat{N} - L)^2$ , i.e., the combined  $k$ -particle and  $-$ hole spaces where  $k = 2, \dots$ , which an extension of our investigation may uncover.

Fig. 8 shows the different components of the von Neumann entanglement entropy, the distillable and the symmetry part. Shown are the distillable entanglement  $S_{\text{vN}}^{\text{dist}}$  in the top row, the symmetry entanglement  $S_{\text{vN}}^{\text{sym}} \equiv -\sum_s p_s \log(p_s)$  in the middle row, and the total von Neumann entropy  $S_{\text{vN}} = S_{\text{vN}}^{\text{dist}} + S_{\text{vN}}^{\text{sym}}$  in the bottom row. The QMBS states are highlighted in red, all results are for  $L = 7$  (odd) and  $L = 8$  (even) lattice sizes, with coupling  $g = 0.9$ . Although the total von Neumann entropy of scar states remains somewhat distinguishable at this coupling, it tends to blend scar states with non-scar states at other couplings, potentially obscuring the scar solutions. This underscores the value of studying entanglement structure—rather than only entanglement entropy—as a more revealing marker to differentiate

scar from non-scar states. Our analytical analysis shows that, because of their stabilizer origin, it is magic that truly differentiates scar from non-scar states.

#### D. Details of the Experimental Realization

In this section of the Supplemental Material, we detail the state-preparation circuits used to generate scar basis states, and discuss additional details. Time evolution is implemented using standard Trotterized circuits, which are well-documented in the literature for this model and are not discussed here.

The experimental procedure discussed in the main text, for odd  $L$ , involves preparing a scar-subspace basis state versus a state outside this subspace, followed by time evolution. To prepare a scar basis state in the LGT a simple circuit, shown in Fig. 3 is employed. The circuit prepares simultaneous  $X_p X_{p+L} = \pm 1$  (represented by  $\prod_{\nu \in p} \sigma_\nu^x \prod_{\nu \in p+L} \sigma_\nu^x$  in the LGT),  $Z_p Z_{p+L} = \pm 1$  (corresponding to  $\sigma_\nu^z$  in the LGT) and Gauss law eigenstates, with eigenvalues chosen according to any of the  $4L$  basis states. The circuit does not introduce horizontal entanglement between qubits, showing the rather trivial entanglement structure of the QMBS basis states; however,

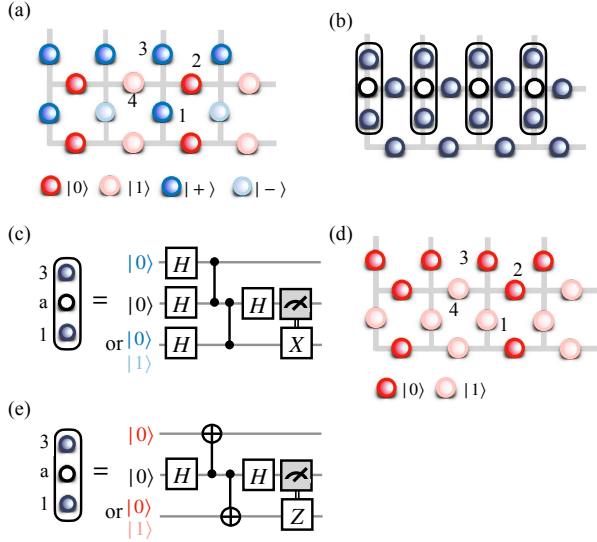


FIG. 9. *Alternative Circuit for QMBS Preparation using mid-circuit measurements.* (a) Initial state for the preparation algorithm in the LGT formulation ( $V_y = 1$ ). Horizontal links are in  $\sigma^z$  (electric) eigenstates, and vertical links in  $\sigma^x$  (magnetic) eigenstates. Alternating  $|0\rangle$  and  $|1\rangle$  (or  $|+\rangle$  and  $|-\rangle$ ) yields eigenstates of any combination of stabilizers  $Z_p Z_{p+L}$  and  $X_p X_{p+L}$ . (b) Mid-circuit measurement-based scheme for simultaneous Gauss law eigenstate preparation using  $L$  ancillas. (c) The circuit measures the combined  $\sigma^z$  parity of two neighboring vertical links via controlled- $\sigma^z$  ( $\Gamma(\sigma^z)$ ) operations and an ancilla  $a$ . The outcome dictates controlled-NOT operations on a vertical qubit, correcting Gauss laws in upper and lower rows, simultaneously. Control instructions classically depend on the desired target scar (via the horizontal links' state) and  $V_y$  sector. (d) A different starting point is shown for the scar state-preparation circuit, a simultaneous eigenstate of the stabilizer  $Z_p Z_{p+L}$  and the Gauss law constraints. (e) This initial state is not eigenstates of an  $X_p X_{p+L}$ ; to transform it into a simultaneous eigenstate, a circuit is used involving mid-circuit measurements and  $L$  ancillas. In a single shot, it measures  $\sigma_\nu^x \sigma_{\nu'}^x$  values, where  $\nu$  and  $\nu'$  denote vertically stacked, vertically oriented links. From this the value of all  $X_p X_{p+L}$  is determined. Based on the measurement outcome and the desired target state, a controlled  $\sigma^z$  operation is applied.

what is noteworthy is that any superposition of these states maintains zero distillable entanglement under time evolution.

An alternative approach, illustrated in Fig. 9(a-e), uses mid-circuit measurements [84, 85, 87] with constant-depth [88–91]. This method is not strictly necessary: Although the model's ground state, the toric code, is long-range entangled for  $g < g_c$ , the scar subspace basis states that span the QMBS eigenstates are simple 2-qubit product states at any coupling (though the QMBS themselves are not). The circuit illustrated in panels (a-c) begins from a state that is an eigenstate of both  $Z_p Z_{p+L}$  and  $X_p X_{p+L}$ , but not of the Gauss law operators. Conversely, the circuit shown in panels (d-e) starts from states that

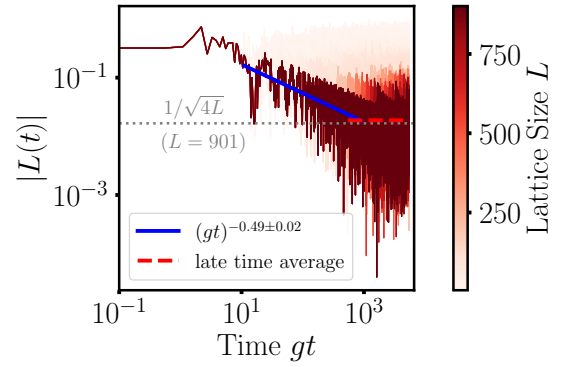


FIG. 10. *Loschmidt echo in the scar subspace for large system sizes  $L$ .* The plot shows the absolute value of the Loschmidt echo,  $|L(t)|$ , evaluated for scar initial states with system sizes up to  $L = 901$ . The echo exhibits a power-law decay,  $\sim (gt)^{-1/2}$ , approaching an asymptotic value of  $1/\sqrt{4L}$  at long times. The fit error is determined by varying the fit range and  $L$ .

are simultaneous eigenstates of both  $Z_p Z_{p+L}$  and the Gauss laws, though not of  $X_p X_{p+L}$ . As in the original method, no entanglement is introduced along the horizontal direction of the lattice, resulting in the same final state.

To create a state outside the scar subspace, a  $z$ -product state that is also a Gauss law eigenstate is initialized. This state will naturally have well-defined  $Z_p Z_{p+L} = \pm 1$  eigenvalues. To ensure it has no non-zero overlap with the scar subspace, the  $Z_p Z_{p+L} = \pm 1$  pattern is carefully chosen.

In this manuscript, we focus on the Loschmidt echo—defined as the overlap between the initial and time-evolved states—and the entanglement of the time-evolved states as key observables. The Loschmidt echo,  $L(t)$ , is a widely used metric to characterize the return probability of time-evolved states and can be measured via an interferometric scheme. This approach involves preparing an ancilla in a Hadamard superposition, using it to control the time-evolution operator, and performing measurements in the  $x$ - and  $y$ - bases to obtain the real and imaginary components of  $L(t)$ , respectively [65–67]. In our analysis, we consider the behavior of  $|L(t)|$  at asymptotic times. On a digital quantum computer this would require Trotterization. Using large Trotter steps risks artificially enhancing the return probability by causing unphysical recurrence to the initial state. Thus very deep circuits are required, which is challenging for near-term devices. Alternatively, instead of its asymptote, one may consider the decay of  $|L(t)|$  at early times which behaves as  $1/\sqrt{gt}$  for an initial state within the scar subspace as shown in Fig. 10 for  $L = 901$ . Computing the same for sufficiently large  $L$ , is classically intractable for a non-scar initial state and is thus not shown here. However, the Loschmidt echo of a thermalizing system should decay exponentially [83].

The distillable entanglement of time-evolved states can

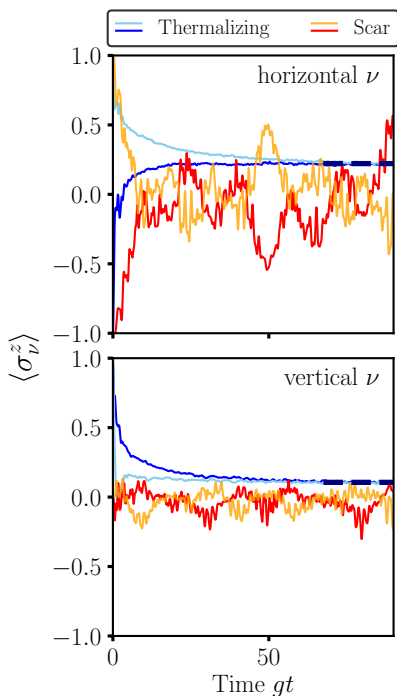


FIG. 11. *Local Observables.* The expectation values of electric operators,  $\langle \sigma_\nu^z \rangle$ , for links oriented horizontally (top panel) and vertically (bottom panel), contrasting scar initial states (red and orange lines) with thermalizing non-scar initial states (dark and light blue lines) for  $L = 9$  and  $g = 0.9$ . For non-scar initial states, the expectation values thermalize to a constant, asymptotic value (indicated by dashed blue lines). In contrast, the expectation values within the scar subspace exhibit oscillatory behavior, albeit without perfect revivals, a consequence of the non-equidistant energy spacing of scar eigenstates. This limits the utility of local observables, as distinguishing these oscillations from finite-volume effects and experimental imperfections may prove challenging. We argue that observables such as the Loschmidt echo or the distillable entanglement, however, allow a stronger distinction between scar and non-scar dynamics.

be measured directly using symmetry-conscious  $k$ -designs that have been proposed in [69], including for the model that is considered here. This scheme enables the measurement of all required quantities such as  $p_s = \text{Tr}(\rho_A^{(s)})$ , as well as  $k$ -fidelities,  $\text{Tr}((\rho_A^{(s)})^k)$ . From these, the distillable von Neumann entropy can be computed using  $S_{\text{vN}}^{(s)} = -\lim_{k \rightarrow 1+} \frac{d}{dk} \text{Tr}((\rho_A^{(s)})^k)$  for sufficiently large  $k$ , typically  $k \approx 3 - 4$  is sufficient [69].

### E. Local Observables

In previous QMBS studies, a more common observable are expectation values of local operators. Fig. 11 shows the behavior of local observables for both scar-subspace initial states and thermalizing states. Specifically, we consider the expectation value of electric operators,  $\langle \sigma_\nu^z \rangle$ ,

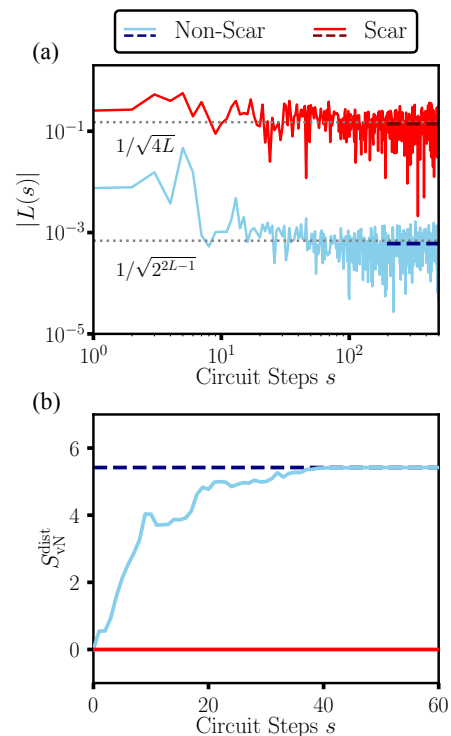


FIG. 12. *Experimental Realization with a Random Circuit.* (a) Evolution of scar and non-scar states through random circuits, as defined in Eq. (55). The absolute value of the Loschmidt echo,  $|L(s)|$ , is shown as a function of the number of circuit steps  $s$ , contrasting an initial state within the scar subspace (red lines) with a state outside this subspace (blue lines) for a system size  $L = 11$ . Dashed lines represent late-time averages. For the scar state, the echo decays to  $|L(s)| \sim 1/\sqrt{4L}$  (gray dotted line), where  $4L$  is the dimension of the scar subspace. Conversely, the non-scar state decays to  $|L(s)| \sim 1/\sqrt{2^{2L-1}}$  (gray dotted line), reflecting the lack of an energy conservation constraint. (b) The distillable entanglement,  $S_{\text{vN}}^{\text{dist}}$ , for scar versus non-scar initial states exhibits similar behavior to that shown in the main text for Hamiltonian evolution.

for horizontal (top panel) and vertical links (bottom panel), comparing scar dynamics (red and orange lines) versus non-scar dynamics (blue and light blue curves). Each panel shows two curves corresponding to horizontal and vertical links at distinct lattice locations. Notably, while scar states exhibit somewhat more pronounced oscillations compared to thermalizing states—where local observables tend toward stationary values—no significant recurrences are observed in the local observables for scar-initial states. This lack of recurrence arises from the non-uniform energy spacing of the scar eigenstates. Because oscillations of similar magnitude may arise from finite-volume effects or experimental imperfections, for instance slight gate over/under rotations vary the value of  $g$  over space and time and additionally smoothen the curves, we believe that local observables offer less contrast between scar and non-scar dynamics than observables like



the Loschmidt echo and distillable entanglement. Future work will include a stability analysis of the scar solutions against experimental imperfections and Trotter evolution.

### F. Random Circuit Evolution

The protocol discussed in the main text compares Hamiltonian evolution within the scar subspace to a thermalizing state outside of it. While valuable from a physics perspective for studying ergodic versus non-ergodic dynamics, it involves Trotterization, which requires very deep circuits to achieve thermalization. To demonstrate a quantum advantage, an alternative is based on shallower randomized circuits. Towards this end, we use the following circuit,

$$\mathcal{U} = \prod_{i=1}^s U(\boldsymbol{\alpha}_i, \boldsymbol{\beta}_i, \boldsymbol{\gamma}_i), \quad (55)$$

where  $s$  is the number of circuit layers, and

$$\begin{aligned} U(\boldsymbol{\alpha}_i, \boldsymbol{\beta}_i, \boldsymbol{\gamma}_i) &\equiv \exp\left\{-\sum_{p=1}^L \alpha_i(p) Z_p Z_{p+L}\right\} \\ &\times \exp\left\{-\sum_{p=1}^L \beta_i(p) [X_p + X_{p+L}]\right\} \\ &\times \exp\left\{-\sum_{p=1}^L \gamma_i(p) [Z_p Z_{p+1} + Z_{p+L} Z_{p+L+1}]\right\}. \quad (56) \end{aligned}$$

The angles  $(\boldsymbol{\alpha}_i, \boldsymbol{\beta}_i, \boldsymbol{\gamma}_i) \equiv (\{\alpha_i(p)\}, \{\beta_i(p)\}, \{\gamma_i(p)\})$  are randomly chosen for every layer, thus the evolution is not constrained by energy conservation as in the main text. In the following we choose  $\alpha_i(p) = \alpha_i$ ,  $\beta_i(p) = \beta_i$ , and  $\gamma_i(p) = \gamma_i$ , i.e., independent of  $p$ , and draw  $(\alpha_i, \beta_i, \gamma_i)$  in every layer from a single-qubit circular unitary ensemble. Other randomizations are also possible.

As in the main text, initial states within the scar subspace remain confined to that subspace under randomized evolution, while states outside it, no longer constrained by energy conservation, explore the full Hilbert space. In Fig. 12, we present the same observables as in our main study: the Loschmidt echo in (a) and the distillable entanglement in (b), both as functions of circuit steps  $s$ . The stark contrast between scar and non-scar dynamics is clearly evident.

We note, however, that many randomized circuits may be classically simulable (see, e.g., [92]) and their computational hardness is an area of active investigation. We believe, therefore, that the thermalization example in the main text thus provides a stronger case for a demonstration of a quantum advantage.